Seasonal characteristics of emission, distribution, and radiative effect of marine organic aerosols over the western Pacific Ocean: an investigation with a coupled regional climate-aerosol model

Jiawei Li[1], Zhiwei Han[1,2*], Pingqing Fu[3], Xiaohong Yao[4], Mingjie Liang[1,2]

[1]CAS Key Laboratory of Regional Climate-Environment for Temperate East Asia (RCE-TEA), Institute of Atmospheric Physics, Chinese Academy of Sciences, Beijing 100029, China

[2]University of Chinese Academy of Sciences, Beijing 100049, China

[3]School of Earth System Science, Tianjin University, Tianjin 300072, China

[4]Laboratory of Marine Environmental Science and Ecology, Ministry of Education, Ocean University of China, Qingdao 266100, China

Correspondence to: Zhiwei Han (hzw@mail.iap.ac.cn)

Abstract: Organic aerosols from marine sources over the western Pacific Ocean of East Asia were investigated by using an online-coupled regional chemistry-climate model RIEMS-Chem for the entire year 2014. Model evaluation against a wide variety of observations from research cruises and in-situ measurements demonstrated a good skill of the model in simulating temporal variation and spatial distribution of particulate matter with aerodynamic diameter less than 2.5 μm and 10 μm ($PM_{2.5}$ and PM_{10}), black carbon (BC), organic carbon (OC), sodium, and aerosol optical depth (AOD) in the marine atmosphere. The inclusion of marine organic aerosols improved model performance on OC concentration by reducing model biases of up to 20%. The regional and annual mean near surface marine organic aerosol (MOA) concentration was estimated to be 0.27 μg m^{-3}, with the maximum in spring and the minimum in winter and contributed 26% of the total organic aerosol concentration on average over the western Pacific. Marine primary organic aerosol (MPOA) accounted for the majority of marine organic aerosol (MOA) mass and MPOA concentration exhibited the maximum in autumn and the minimum in summer, whereas marine secondary organic aerosol (MSOA) was approximately 1~2 orders of magnitude lower than MPOA, having a distinct summer maximum and a winter minimum. MOA induced a direct radiative effect (DRE_{MOA}) of -0.27 W m^{-2}, and an indirect radiative

effect (IRE$_{MOA}$) of -0.66 W m^{-2} at TOA (IRE$_{MOA}$) in terms of annual and oceanic average over the western Pacific, with the highest seasonal mean IRE$_{MOA}$ up to -0.94 W m^{-2} in spring. IRE$_{MOA}$ was stronger than but in a similar magnitude to the IRE due to sea salt aerosol on average, and it was approximately 9% of the IRE due anthropogenic aerosols in terms of annual mean over the western Pacific, and this ratio increased to 19% in the northern parts of the western Pacific in autumn. This study reveals an important role of MOA in perturbing cloud properties and shortwave radiation fluxes in the western Pacific of East Asia.

1 Introduction

Atmospheric aerosol is one of the most important and uncertain factors in climate change issues (IPCC, 2013). Aerosols can alter radiation balance by scattering/absorbing solar/infrared radiation, and affect cloud microphysics and lifetime by activating as cloud condensation nuclei (CCN), exerting significant effects on climate system directly and indirectly. Aerosols are originated from anthropogenic and natural sources and of high spatial and temporal variability and short atmospheric lifetime relative to greenhouse gases. Consequently, aerosol radiative and climatic effects often have strong regional characteristics.

The western Pacific Ocean is frequently influenced by continental outflow of both anthropogenic and natural aerosols. Due to continuous growth of economy and energy consumption in the past decades, the aerosol level in China has been enhanced (Smith et al., 2011; Li M. et al., 2017) and may have potentially significant effects on radiation and cloud over not only the East Asian continent but also the wide downwind oceanic areas. Besides, East Asia is one of the major dust source regions on earth (Shao and Dong, 2006). Dust storms often occur in spring and dust particles can be transported eastward from the deserts and Gobi areas of north China and southern Mongolia to the western Pacific Ocean (Gong et al., 2003), providing nutrients (e.g., iron) for phytoplankton or even triggering the outbreak of algae bloom in oceans (Calil et al., 2011; Tan et al., 2017). In addition to anthropogenic and dust aerosols, marine aerosols also significantly affect aerosol chemical composition, radiation transfer, and cloud properties in marine atmosphere. The behaviors and climatic impacts of sea salt and non-sea-salt sulfate oxidized from dimethylsulphide (DMS) have been extensively investigated (Graf et al., 1997; Liao et al., 2004; Rap et al., 2013). In recent years, particular attentions have been paid on the sources and impacts of marine organic aerosols (O'Dowd et al., 2004; Meskhidze and

Nenes, 2006; Luo and Yu, 2010; Vignati et al., 2010; Gantt et al., 2011; Burrow et al., 2014; Quinn et al., 2017; Bertram et al., 2018; Huang et al., 2018), however, such studies were still very limited, especially for the western Pacific.

O'Dowd et al. (2004) found that organic matter dominated the chemical composition of marine aerosol during plankton bloom periods from spring to autumn over the North Atlantic Ocean, contributing 63% to sub-micron aerosol mass. Meshkidze and Nenes (2006) revealed a significant impact of phytoplankton bloom on cloud droplet number concentration and radiation balance in the Southern Ocean and proposed a major contribution of secondary organic aerosol (SOA) from phytoplankton produced isoprene. Some studies indicated that primary marine sources may dominate marine organic matter, whereas SOA oxidized from marine isoprene could only comprise a small fraction of the observed organic aerosol mass over marine environment (Facchini et al. 2008; Arnold et al., 2009; Myriokefalitakis et al., 2010). The estimated global emission amounts of primary marine organic matter varied largely among models. Using the global aerosol-climate model ECHAM5-HAM, Roelofs (2008) estimated a global production of marine organic aerosols to be 75 TgC yr^{-1}. Spracklen et al. (2008) estimated the marine organic carbon emission to be approximately 8 TgC yr^{-1} based on measured organic carbon mass and satellite retrieved chlorophyll-a (Chl-a) concentration. Vignati et al. (2010) derived a global emission of marine primary organic matter in the sub-micron size by sea spray process to be 5.8 TgC yr^{-1} by using an off-line global Chemistry-Transport Model TM5 with a parameterization relating organic emission fraction to sea surface Chl-a concentration. Gantt et al. (2011) found that the combination of 10 m wind speed and sea surface Chl-a concentration were the most consistent predictors of organic mass fraction of sea spray aerosol based on observations from the Mace Head atmospheric research station on the Atlantic coast of Ireland and a site at the Point Reyes National Seashore on the Pacific coast of California. They developed a new MPOA emission function and estimated the global annual MPOA emission associated with sea spray to be from 15.9 TgC yr^{-1} to 18.7 TgC yr^{-1} (2.8~5.6 TgC yr^{-1} in the sub-micron size). However, Quinn et al. (2014) found that the organic carbon content of sea spray aerosol is weakly correlated with satellite retrieved chlorophyll-a concentration based on cruise measurements in the North Atlantic Ocean and the coastal waters of California. Bates et al (2020) reported that plankton bloom has little effect on the emission flux, organic fraction or cloud condensation nuclei of sea spray aerosol based on cruise experiment over the North Atlantic. Burrows et al. (2014) developed a novel physically based framework for

parameterizing the organic fractionation of sea spray aerosol by consideration of ocean biogeochemistry processes, and their predicted relationships between Chl-a and organic fraction are similar to existing empirical parameterizations associated with ocean Chl-a concentrations at high Chl-a levels, but the empirical relationships may not be adequate to predict OM fraction of sea spray aerosol outside of strong seasonal blooms.

Regarding the influence on climatic factors, such as cloud condensation nuclei (CCN), Ovadnevaite et al. (2011) revealed that MPOA was a dichotomy of low hygroscopicity and high CCN activity through analysis of ambient measurements of aerosol chemical compositions and size distributions at the Mace Head atmospheric research station, and highlighted the importance of MPOA in CCN activation over marine atmosphere. A later study of Westervelt et al. (2012) indicated that marine organic aerosols was able to increase CCN by up to 50% in the Southern Ocean and by 3.7% globally during the austral summer based on the model simulation of GISS GCM II'. Based on the measurements from seven research cruises over the Pacific, Southern, Arctic, and Atlantic oceans between 1993 and 2015, Quinn et al. (2017) indicated that sea spray aerosol generally makes a contribution of less than 30% to CCN population at supersaturation of 0.1 to 1.0% on a global basis. Burrows et al. (2022) pointed out that sea spray organic aerosol strengthened shortwave radiative cooling by clouds by -0.36 Wm^{-2} in the global annual mean, with the zonal mean contribution exceeding -3.5 W m^{-2} in the Southern Ocean in summertime.

The above studies reveal the important role of marine organic aerosols in chemical composition, radiation budget, and cloud microphysics with focus on the global scale. However, there is very limited modeling research on this important and challenging issue for the western Pacific Ocean of East Asia. To our knowledge, only two of our previous studies explored the effects of MPOA on chemical composition, radiation, cloud and precipitation over the western Pacific in springtime with an online-coupled regional chemistry/aerosol-climate model RIEMS-Chem (Han et al., 2019; Li et al., 2019), whereas the seasonality and annual aspect of MPOA and MSOA produced by marine isoprene and terpene are still unknown. In this study, we conducted a one-year simulation with the developed RIEMS-Chem to further explore the characteristics and radiative impacts of marine organic aerosols over the western Pacific. The model simulated aerosol compositions were validated against a wide series of observations from ground and cruise measurements, and the simulated MSOA was evaluated by comparison with cruise measured secondary organic tracer in marine air masses. To our knowledge,

121 for the first time, the seasonality of emissions, concentrations, direct and indirect radiative effects of

122 marine organic aerosols was characterized and the annual means were estimated specifically for the

123 western Pacific and for the key oceanic regions of concern over East Asia. This study would provide

124 new insights into properties and impacts of marine organic aerosols over the western Pacific and

125 would be a necessary supplement to the global perspective of marine organic aerosols.

126

127 2 Model and data

128 2.1 Model description and key processes

129 An online-coupled regional atmospheric chemistry/aerosol-climate model RIEMS-Chem was

130 used to investigate marine organic aerosols in this study. RIEMS-Chem composes of the host regional

131 climate model RIEMS (Fu et al., 2005; Xiong et al., 2009; Wang S.Y. et al., 2015) and a

132 comprehensive atmospheric chemistry/aerosol module. RIEMS was developed based on the dynamic

133 structure of the fifth-generation Pennsylvania State University NCAR Mesoscale Model (MM5; Grell

134 et al., 1995) with a series of parameterizations to represent major physical processes, such as a

135 modified Biosphere-Atmosphere Transfer Scheme (BATS; Dickinson et al., 1993) for land-surface

136 process, the Medium-Range Forecasts scheme (MRF; Hong and Pan, 1996) for planetary boundary

137 layer process, the Grell cumulus convective parameterization scheme (Grell, 1993) for convective

138 process, the Reisner explicit moisture scheme (Reisner et al., 1998) and a modified radiation package

139 of the NCAR Community Climate Model (CCM3; Kiehl et al., 1996) for radiation transfer processes

140 with aerosol effect. RIEMS has participated in the Regional Climate Model Intercomparison Project

141 (RMIP) for Asia and it was one of the best models in predicting surface air temperature and

142 precipitation over East Asia (Fu et al., 2005).

143 Atmospheric chemistry/aerosol modules have been incorporated into RIEMS in recent years,

144 establishing the online-coupled model RIEMS-Chem, which can account for the interactions among

145 chemistry, radiation, cloud, and meteorology (Han, 2010; Han et al., 2012). RIEMS-Chem has been

146 successfully applied in previous modeling studies on anthropogenic aerosols, mineral dust and marine

147 aerosols regarding spatial-temporal distributions, physical and chemical evolutions, and radiative and

148 climatic effects over East Asia (Han et al., 2012; 2013; 2019; Li et al., 2014; 2016a; 2016b; 2019;

149 2020). It is now participating in the international model comparison project MICS-Asia III (Model

150 Inter Comparison Study for Asia phase III) and shows a good ability in predicting aerosol

concentrations and AOD over East Asia (Gao et al., 2018).

RIEMS-Chem includes atmospheric chemistry and aerosol processes, such as gas and aqueous phase chemistries which are represented by the CB-IV mechanism (Gery et al. 1989) and RADM scheme (Chang et al., 1987), respectively; Sulfate is mainly produced from the oxidation of SO_2 by OH radical in gas phase and the oxidation of dissolved SO_2 by H_2O_2, O_3, and metal catalysis in aqueous phase (Chang et al., 1987). Nitrate and ammonium are produced through thermodynamic processes represented by the ISORROPIA II model (Fountoukis and Nenes, 2007). BC, POA, and anthropogenic primary PMs are considered chemically inert. SOA formation from anthropogenic and biogenic VOC precursors is treated by a bulk yield scheme from Lack et al. (2004), with SOA yield of 424 $\mu g\ m^{-3}\ ppm^{-1}$ for toluene, 342 $\mu g\ m^{-3}\ ppm^{-1}$ for xylene, and 762 $\mu g\ m^{-3}\ ppm^{-1}$ for monoterpene. For irreversible conversion of marine VOCs to SOA, a 28.6% mass yield is assumed for isoprene (Surratt et al., 2010, Meskhidze et al., 2011) and 30% for monoterpene (Lee et al., 2006). Heterogeneous reactions between gaseous precursors and aerosols are also taken into account (Li and Han, 2010; Li J. W. et al., 2018). Dry deposition velocity is represented by a size-dependent parameterization over different underlying surfaces (Han et al., 2004). Dry deposition velocity of particle is expressed as the inverse of the sum of resistant plus a gravitational settling term. Over sea or ocean surfaces, the quasi-laminar boundary layer (QBL) may be disrupted by bursting bubbles, resulting in an increase in downward movement of particles, which is parameterized by the approach of Van den Berg et al. (2000), in which quasi-laminar resistance r_b is determined by Brownian diffusion and impaction when QBL is intact, and by turbulence and washout velocity of particles by spray drops when QBL is broken down. Below-cloud scavenging (BCS) of particles between cloud base and ground surface represents capture processes of particle by falling hydrometeor through Brownian and turbulent shear diffusion, interception and inertial impaction, and is parameterized by a scavenging rate, which is a function of precipitation rate and collision efficiency of particle by hydrometeor (Slinn, 1984).

A physically based scheme (namely A-G scheme) developed based on classical Köhler theory by Abdul-Razzak and Ghan (1998, 2004) is incorporated into RIEMS-Chem to represent aerosol activation into cloud droplet processes. This scheme calculates cloud droplet number concentration (N_c) with not only aerosol number concentration, but also aerosol size distribution and composition, updraft velocity and ambient supersaturation. Aerosols are activated if their critical supersaturation is

181   less than the maximum ambient supersaturation. The critical supersaturation for activating particles is

182   determined by curvature effect and solute effect. The maximum ambient supersaturation is calculated

183   by solving supersaturation balance equation (Abdul-Razzak and Ghan, 1998). The updraft velocity is

184   represented by the sum of grid mean updraft velocity and sub-grid updraft velocity, which is

185   diagnosed from vertical eddy diffusivity according to Ghan et al. (1997). The A-G scheme in

186   RIEMS-Chem has been applied over the western Pacific Ocean in spring 2014 and its prediction for

187   hourly CCN concentration at different supersaturations has been validated by cruise measurements

188   from the marginal seas of China to remote oceans southeast of Japan, which demonstrates a good

189   ability, with the correlation coefficient of 0.87 and normalized mean bias within 20%. More details on

190   the treatment and evaluation of marine aerosol activation refer to Han et al. (2019). Once N_c is

191   calculated by the A-G scheme, the cloud droplet effective radius r_e is calculated with the method of

192   Martin et al. (1994). The activated aerosols (into cloud droplet) are removed from the air. The auto

193   conversion rate from cloud water to rainwater is parameterized by the scheme of Beheng (1994),

194   which depends on N_c diagnosed and cloud liquid water content. The effect of aerosols on ice nuclei

195   and convective cloud is not treated in this model due to limited knowledge at present.

196

197   2.2 Aerosol physical and chemical properties

198   Ten aerosol types are simulated in RIEMS-Chem, which are sulfate (SO_4^{2-}), nitrate (NO_3^-),

199   ammonium (NH_4^+), black carbon (BC), primary organic aerosol (POA), secondary organic aerosol

200   (SOA), anthropogenic primary PMs ($PM_{2.5}$ and PM_{10}), dust, and sea salt.

201   Based on the observational analysis of aerosol mixing state in eastern China (Ma et al., 2017; Wu

202   et al., 2017), an internal mixing assumption is adopted for anthropogenic aerosols and they are

203   externally mixed with natural aerosols. The geometric mean radius and standard deviation of the

204   anthropogenic internal mixture are estimated to be 0.11 μm and 1.65, respectively, based on field

205   measurements (Ma et al., 2017). Mineral dust is represented by 5 size bins (0.1~1.0, 1.0~2.0, 2.0~4.0,

206   4.0~8.0 and 8.0~20.0 μm), while sea salt is represented by 2 size bins, with the mean fine mode radius

207   being 0.1μm and the coarse mode radius being 1 μm according to measurements from Gong et al.

208   (1997). Feng et al. (2017) indicated that the measured total organic carbon (TOC) in the western

209   Pacific Ocean during the same period as this study was enriched in <0.3 μm (volume median

210   diameter), which was mainly contributed by MPOA and the super-micron TOC was generally below

211 the detection limit. Accordingly, the geometric mean diameter of marine organic aerosol number

212 concentration was set to be 0.1 μm, with a standard deviation of 1.6. The number concentration is

213 calculated by mass concentration as the formula in Curci et al. (2015). MPOA can be mixed with sea

214 salt both externally or internally. It is more likely to be externally mixed with sea salt for finer

215 aerosols (<200 nm in diameter) (Gantt and Meskhidze, 2013) and the effect of externally mixed

216 MPOA was found to be much more important than that of internally mixed MPOA (Gantt et al.,

217 2012b). So an external mixture of MPOA and sea salt is assumed in this study, this means additional

218 marine organic aerosols are produced to affect cloud properties and represents an upper limit of

219 indirect effect. There is little information on physical and chemical properties of marine organic

220 aerosols, some key parameters for calculation of aerosol activation, i.e. the number of ions the salt

221 dissociates into water, the osmotic coefficient, the mass fraction of soluble material, the density, and

222 molecular weight are set to be 3.0, 1, 0.1, 1.5 g m^{-3}, and 90, respectively, according to a few previous

223 studies (Abdul-Razzak and Ghan, 2004; Roelofs, 2008). The soluble mass fraction of MSOA is

224 assumed to be 0.2, slightly higher than that of MPOA (Liu and Wang, 2010; Westervelt et al., 2012).

225 An OM/OC ratio of 1.4 was applied to convert organic matter (OM) to OC (Gantt and Meskhidze,

226 2013).

227   The hygroscopic growth of aerosol is parameterized by a κ parameterization (Petters and

228 Kreidenweis, 2007). The hygroscopicity parameters (κ) for inorganic aerosol components, BC, POA,

229 SOA, dust, and sea salt are set to be 0.65, 0, 0.1, 0.2, 0.01 and 0.98, respectively (Riemer et al., 2010;

230 Liu et al., 2010; Westervelt et al., 2012). The hygroscopicity for MPOA and MSOA are assumed to be

231 the same as those for anthropogenic POA and SOA. Because there was limited information on the

232 optical properties of marine organic aerosols, the refractive index of anthropogenic POA and SOA was

233 used instead. The aerosol refractive index and hygroscopicity (κ) of the internally mixed aerosol are

234 calculated by volume-weighting of the parameters for each aerosol component. Aerosol optical

235 parameters including extinction coefficient, single scattering albedo, and asymmetry factor are

236 calculated by a Mie-theory based method developed by Ghan and Zaveri (2007), in which the aerosol

237 optical parameters are pre-calculated by the Mie theory and then fitted by Chebyshev polynomials

238 with a table of polynomial coefficients for looking up for aerosols with certain size and refractive

239 index. More detailed description refers to Li et al. (2020). This approach is much faster than

240 traditional Mie code with a similar level of accuracy and has been successfully used in estimating

241   aerosol optical properties over East Asia (Han et al. 2011).

242

243   2.3 Anthropogenic and natural emissions

244   Monthly mean anthropogenic emissions of sulfur dioxide (SO_2), nitrogen (NO_x), ammonia (NH_3),

245   non-methane volatile organic compounds (NMVOC), carbon monoxide (CO), BC, POA, and other

246   anthropogenic primary $PM_{2.5}$ and PM_{10} in China for the year 2014 are obtained from the MEIC

247   inventory (Multi-resolution Emission Inventory for China) which was developed by Tsinghua

248   University (http://meicmodel.org, last access: 2020/01/20). Anthropogenic emissions outside China

249   are taken from the MIX inventory which was developed to support the Model Inter-Comparison Study

250   for Asia phase III (MICS-Asia III) and the Hemispheric Transport of Air Pollution (HTAP) projects

251   (Li M. et al., 2017). Both inventories of MEIC and MIX have the same resolution of 0.5 degree. Open

252   biomass burning emissions of aerosols and gas precursors for the year 2014 with a spatial resolution

253   of 0.5 degree are derived from the Global Fire Emissions Database, Version 4.0 (GFED4) on a daily

254   basis (Giglio et al., 2013). The biogenic VOC emission is derived from the CAMS-BIO Global

255   biogenic emissions dataset (CAMS-GLOB-BIO v3.1) (Granier et al., 2019; Sindelarova et al., 2014)

256   distributed by ECCAD-GEIA (https://permalink.aeris-data.fr/CAMS-GLOB-BIO, last access:

257   2020/02/10) and the monthly mean biogenic emission for the year 2014 with a horizontal resolution of

258   0.25° is used. All the above emission data are bilinearly interpolated to the lambert projection of

259   RIEMS-Chem. The deflation of mineral dust is represented by the scheme of Han et al. (2004), which

260   is calculated online with RIEMS predicted meteorology.

261   The generation of sea salt aerosol through bubbles is represented by Gong (2003) which is

262   developed for sea salt radius from 0.07μm to 20μm based on the scheme of Monahan et al. (1986) and

263   it is modified by considering the influences of relative humidity (RH) (Zhang et al., 2005).

264   Considering the strong bloom seasonality in the western Pacific region and the availability of

265   global satellite data for Chl-a concentration, and the lack of cruise measurements on the relationship

266   between sea spray organic aerosol fluxes and Chl-a in this region, we adopted the scheme of Gantt et

267   al (2011) for parameterizing marine primary organic aerosol emission in this study. The size-resolved

268   marine primary organic aerosol (MPOA) emission is parameterized based on the method of Gantt et al.

269   (2011; 2012a), in which the emission rate of MPOA is the product of sea spray emission rate and

270   organic matter fraction of sea spray aerosol, which is expressed as a function of wind speed, surface

271 seawater Chl-a concentration, and aerosol size. The Chl-a data used in this study is the Level-3 daily

272 mean Chl-a concentration (mg m^{-3}) product with 9 km resolution retrieved from the VIIRS (Visible

273 infrared Imaging Radiometer) sensor onboard the Suomi National Polar-orbiting Partnership (SNPP)

274 satellite platform (OBPG, 2018) (http://oceandata.sci.gsfc.nasa.gov, last access: 2020/12/8). A brief

275 description on this scheme with formulas is presented in the supplement.

276   Marine isoprene emission released by phytoplankton activities is parameterized using the scheme

277 of Gantt et al. (2009) which considers light sensitivity of phytoplankton isoprene production and

278 dynamic euphotic depth (see more details in the supplement). Marine emission of monoterpene is

279 scaled by 0.2 to those of isoprene following the suggestion from Myriokefalitakis et al. (2010). The

280 marine abiotic source of isoprene (due to photochemical production in the sea surface microlayer)

281 may be important according to recent studies (Brüggemann et al., 2018; Conte et al., 2020). This

282 mechanism is not considered in this study because the production mechanism for marine abiotic

283 isoprene is poorly understood at present.

284

285 2.4 Model setup and experiment design

286   This study focused on the western Pacific Ocean of East Asia. The model domain covered most

287 areas of eastern China, the Korean Peninsula, Japan, parts of Southeast Asia, and a wide area of the

288 western Pacific Ocean (11°N~54°N, 89°E~173°E) (Figure 1). A lambert conformal projection with 60

289 km horizontal resolution was applied in the model. 16 vertical layers stretched unevenly from the

290 surface to tropopause in a terrain-following sigma coordinate with the first 8 layers within planetary

291 boundary layer. The time step of model integration is 180 seconds. The simulation period was from 1

292 December 2013 to 31 December 2014 with the first month as model spin-up and the whole year of

293 2014 was used for analysis. Year 2014 is a normal year (neither El Niño nor La Niña) which can be

294 reflected by the ENSO index (https://psl.noaa.gov/enso/mei/, last access: 2023/12/15). The reason we

295 choose 2014 as the study period is the availability of cruise campaigns (for model validation and

296 analysis) over the East China Sea and the western Pacific from spring to early summer, when BC and

297 OC concentrations were measured. Final reanalysis data with 1°×1° resolution and 6-hour interval

298 from the National Centers for Environmental Prediction (NOAA/NCEP, 2000) was used to provide

299 initial and boundary conditions for meteorology. Chemical results derived from the MOZART-4

300 (Model for Ozone and Related chemical Tracers, version 4; Emmons et al., 2010) simulation with

301   6-hour interval were used to provide lateral conditions for trace gases and aerosols. The full

302   simulation (FULL) is designed by considering all anthropogenic and natural emissions, including

303   marine emissions of primary organic aerosol and sea salt, and a series of model simulations are also

304   conducted to estimate the direct and indirect radiative effect of MOA and their sensitivity to MOA

305   properties, which are described in the following sections.

306

307   2.5 Observations

308   In-situ measurements of PM_{10}, $PM_{2.5}$, and gas precursors (O_3, SO_2, and NO_x/NO_2) at coastal and

309   island sites in Japan and Republic of Korea were obtained from EANET (Acid Deposition Monitoring

310   Network in East Asia, http://www.eanet.asia, last access: 2020/01/23) (Figure 1). Hourly

311   concentrations of PM_{10}, SO_2, NO_x in Japan, NO_2 in Korea, and O_3 were automatically monitored at

312   six Japanese sites (Rishiri, Tappi, Sado-seki, Oki, Hedo, and Ogasawara) and three Korean sites (Jeju,

313   Kanghwa, and Imsil), whereas hourly $PM_{2.5}$ concentrations were only available at three Japanese sites

314   (Rishiri, Sado-seki, and Oki). Sodium (Na^+) concentrations sampled on a bi-weekly basis at the 6

315   coast/island EANET sites in Japan were also collected. Besides, hourly PM_{10} and $PM_{2.5}$

316   concentrations monitored in the three coastal cities of China (Qingdao, Shanghai, and Fuzhou) were

317   also obtained from the CNEMC (China National Environmental Monitoring Center,

318   http://www.cnemc.cn/, last access: 2020/01/23) and used for model validation (Figure 1).

319   Carbonaceous aerosol (OC and BC) concentrations measured from two research cruise campaigns

320   covering the western Pacific during the spring and summer of 2014 (Figure 1) were collected and used

321   for model validation. The spring cruise campaign was carried out from 17 March to 22 April 2014

322   onboard the research vessel R/V Dongfanghong II, which started from Qingdao, sailed to the western

323   Pacific Ocean, and then returned (Figure 1) (Luo et al., 2016; Feng et al., 2017). OC and BC samples

324   were collected by an 11-stage MOUDI (Models110-IITM) (0.054~18 μm) equipped with

325   pre-combusted quartz filters onboard the vessel. Mass concentrations of total OC (primary and

326   secondary) and BC were determined by the thermal/optical carbon analyzer (Sunset Laboratory Inc.,

327   Forest Grove, OR). Totally 19 daily BC and OC samples were collected during the cruise. Detailed

328   information about this campaign and the sampling and analysis techniques were documented in Feng

329   et al (2017). The early summer campaign was carried out from 18 May to 12 June 2014 (Kang et al.,

330   2018). Total suspended particles (TSP) were collected on pre-combusted quartz filters using a

high-volume air sampler (Kimoto, Japan) onboard the KEXUE-1 Research Vessel during a National Natural Science Foundation of China (NSFC) sharing cruise (Figure 1). This campaign covered low- to mid-latitudes of the western Pacific Ocean (over the Yellow Sea and the East China Sea). Totally 51 half-day (daytime/nighttime) OC samples were obtained during this campaign. Detailed information about this campaign and samples were described in Kang et al. (2018).

Besides the in-situ observations and cruise campaigns mentioned above, long-term observations of OC and BC from previous publications were collected to help model comparison and analysis. Carbonaceous aerosol samples (OC and BC) in TSP were continuously collected on a weekly basis from 2001 to 2012 at Chichijima Island (the same place as Ogasawara in Figure 1), a remote island located in the western North Pacific. The monthly mean OC and BC concentrations of the 12-year average were reported by Boreddy et al. (2018) and used to verify the model performance over remote oceans. Measurements of seasonal mean OC and BC concentrations in TSP at Huaniao Island (a pristine island about 100 km southeast of Shanghai over the East China Sea, see Figure 1) from October 2011 to August 2012 (Wang F. W. et al., 2015) and at Okinawa island (the same place as Hedo in Figure 1) in the western Pacific Ocean from October 2009 to October 2010 (Kunwar and Kawamura, 2014) were collected and used in this study. BC observations were conducted at Fukue Island of western Japan using a continuous soot-monitoring system (COSMOS) (Figure 1) by Kanaya et al. (2016) from 2009 to 2015.

Ground observations of AOD were obtained from the Aerosol Robotic Network (AERONET, https://aeronet.gsfc.nasa.gov/, last access: 2020/06/03). Level 2 AOD observations for the year 2014 were collected at 7 coastal sites shown in Figure 1. Hourly and monthly mean observations were derived from raw data and used for model comparison and statistics calculation. AOD at 550 nm was used to match the model output. The level-3, daily deep blue global AOD product (in $1° \times 1°$ horizontal resolution and at 550nm) retrieved by VIIRS sensor onboard the SNPP satellite platform (Sayer et al. 2018) were also collected to examine AOD spatial distribution.

3 Model validations

In this section, the model results for OC, BC, PM_{10}, $PM_{2.5}$, sodium concentrations, and AOD were compared with a variety of observations from research cruise and monitoring networks to help evaluate the model ability over wide areas from eastern China to the western Pacific Ocean. Because

361 the above comparison was for total OC mass concentration, we also compared the simulated SOA

362 from marine sources to cruise measured SOA tracer to examine the model performance for marine

363 organic aerosols. Model results are extracted from the model grid closest to the observational site for

364 comparison with observations.

365

366 3.1 Particulate matters (PM_{10} and $PM_{2.5}$), sodium (Na^+) and gas precursors

367   As particulate matter in remote marine atmosphere is mainly composed of sea salt, the model

368 performance for PM_{10} and $PM_{2.5}$ may partly reflect the model ability for sea salt simulation, which is

369 crucial to the estimation of MPOA emission.

370   Because the focus of this study is seasonal variation, the hourly PM_{10} and $PM_{2.5}$ observations and

371 corresponding simulations were averaged to be monthly means and shown in Figure 2. In general,

372 RIEMS-Chem performed quite well in simulating monthly variation of PM_{10} concentrations at both

373 the EANET sites (Figure 2a~2i) and CNEMC sites (Figure 2j~2l) for the year 2014, although model

374 biases still occurred at some sites, such as the underprediction in winter and spring in Jeju (Figure 2g)

375 and Imsil (Figure 2i) and the overprediction in May in Oki (Figure 2d) and Rishiri (Figure 2a). It was

376 striking that PM_{10} concentration peaked in May and was lowest in July-August at all Korean sites and

377 Japanese sites over northeast Asia (Figure 2a~2i). The long-range transport of mineral dust from north

378 China and Mongolia in spring could contribute to the PM_{10} maximum in May. It was noteworthy that

379 the model simulated seasonality and magnitude of PM_{10} agreed quite well with observations at the

380 four island sites of northern Japan (Rishiri, Tappi, Sado, and Oki) (Figure 2a~2d), where sea salt

381 aerosol played a more important role than those sites in Korea, implying sea salt concentrations could

382 also be well reproduced by the model. The PM_{10} level at Ogasawara (Figure 2f) was much lower than

383 those at the other sites and its seasonality was characterized by the minimum in summer (5 $\mu g\ m^{-3}$)

384 and the maximum in spring. The model reasonably reproduced the seasonality at Hedo (Figure 2e) and

385 Ogasawara (Figure 2f) as well, although it generally predicted lower values at Hedo and higher values

386 at Ogasawara. As for PM_{10} concentrations at the CNEMC sites of eastern China, the model simulated

387 PM_{10} concentrations very well for Shanghai (Figure 2k) and Fuzhou (Figure 2l) in terms of both

388 monthly variation and magnitude, showing higher values in spring and the maximum in winter in

389 Shanghai, and an almost stable level around 60 $\mu g\ m^{-3}$ in Fuzhou throughout the year except for the

390 elevated value in January. The PM_{10} level in Qingdao (Figure 2j) was higher than those in Shanghai

and Fuzhou, and reached the maximum of 170 μg m^{-3} in January due to anthropogenic sources and the peak in March was resulted from the effect of mineral dust.

The monthly variations of PM$_{2.5}$ concentrations at Rishiri, Sado, and Oki (Figure 2m~2o) were similar to those of PM$_{10}$, but the peaks in May were not as evident as those of PM$_{10}$, because mineral dust comprises a small fraction of fine particles and has less effect on PM$_{2.5}$ variation. The model reproduced PM$_{2.5}$ concentrations very well at the three coastal sites of eastern China (Figure 2p~2r) and the monthly variation of PM$_{2.5}$ concentrations resembled those of PM$_{10}$, because fine particle accounts for a large fraction of PM mass in these Chinese megacities due to the dominant effect of anthropogenic sources.

Aerosol chemical components including primary anthropogenic PM, sea salt, mineral dust, MOA, anthropogenic carbonaceous aerosols (BC+OC), and inorganic aerosols (sulfate+nitrate+ammonium) in PM$_{10}$ and PM$_{2.5}$ at all the EANET and CNEMC sites are also shown in Figure 2. It is found that sea salt dominated PM$_{10}$ mass at the coastal and island sites of Japan and Korea in most months except May and June when dust aerosols were abundant (Figure 2a~2g). MOA accounted for a small fraction of PM$_{10}$ mass at all sites, however, the relative contribution of MOA to PM$_{2.5}$ mass appeared to be larger than that of sea salt at the coastal sites of Japan (Figure 2m~2o), indicating the potential importance of MOA in fine aerosol mode in marine atmosphere.

Table 1 shows that for all the 9 EANET sites, the overall mean PM$_{10}$ concentration was 30.0 μg m^{-3} from observation and 28.5 μg m^{-3} from simulation, with the overall Pearson correlation coefficient (R) of 0.65 (0.48~0.64) and the normalized mean bias (NMB) of -5% (-27~36%). For PM$_{2.5}$, the mean concentrations averaged over the EANET sites were 10.9 μg m^{-3} from observation and 12.3 μg m^{-3} from simulation, with R and NMB of 0.61 (0.53~0.64) and 12% (0~21%), respectively. The annual mean observed and simulated PM$_{10}$ concentrations at the 3 CNEMC sites (Table 2) were 81.6 μg m^{-3} and 80.7 μg m^{-3}, with R and NMBs of 0.65 (0.38~0.61) and -1% (-4~1%), respectively, while the annual mean observed and simulated PM$_{2.5}$ concentrations, R, and NMB were 46.6 μg m^{-3}, 43.4 μg m^{-3}, 0.70 (0.44~0.72), and -7% (-12~0%), respectively. The good performance statistics shown in Table 1 and Table 2 suggest a good skill of RIEMS-Chem in reproducing PM levels from the coastal regions of east China to the remote western Pacific. Figure 2, Table 1, and Table 2 also illustrate that the spatial distribution of PM exhibited higher concentrations at the continental (coastal) sites (CNEMC sites, Jeju, Kanghwa, and Imsil) and lower concentrations at the remote island site

(Ogasawara) over the western Pacific, which were also reasonably reproduced by RIEMS-Chem.

Seasonal mean statistics of PM_{10} and $PM_{2.5}$ concentrations at the EANET and CNEMC sites were also listed in Table 1 and Table 2. Statistics for spring (March-April-May, MAM), summer (June-July-August, JJA), autumn (September-October-November, SON), and winter (December-January-February, DJF) were calculated. PM_{10} observations generally exhibited higher concentrations in MAM and DJF, moderate concentrations in SON, and lower concentrations in JJA at most sites covering coastal areas (CNEMC sites, Jeju, Kanghwa, and Imsil) and remote islands (e.g. Oki, Hedo, and Ogasawara). The model reproduced such seasonal variation of PM_{10} reasonably well although some underestimations occurred from winter to spring at Jeju and Imsil (Figure 2g, 2i), which could be attributed to the uncertainties in emissions (anthropogenic, biomass burning).

Comparison with observations of Sodium (Na^+) concentration at 6 Japan coastal/island sites from EANET is conducted to further examine the model performance for sea salt. The modeled sodium is estimated to be 38.56% of sea salt mass (Kelly et al., 2010), and the agreement between observation and model simulation is generally satisfactory at all sites except at Oki in December, when the model largely underpredict Na^+. The model well reproduces the seasonality of sodium concentration, with the maximum in winter and the minimum in summer (Figure 3). The model predicts sodium concentration best at Ogasawara, with the correlation coefficient of 0.85 and NMB of 5%. The overall correlation coefficient for all sites is 0.50, with NMB of -11% (Table S1).

In all, RIEMS-Chem was able to reasonably reproduce the spatial distribution and seasonal variation of PM_{10}, $PM_{2.5}$, and sodium concentrations in the marine environment of the western Pacific. The above good performances give us confidence in the estimation of marine sea salt emission.

In addition, the overall statistics were generally acceptable for gas precursors (O_3, SO_2, and NO_x/NO_2), indicating atmospheric chemistry processes could be reasonably represented by the model over the western Pacific. (see statistics in Table S2)

3.2 Carbonaceous aerosols

Modeled BC and OC concentrations were compared with observations from research cruises and from previous publications at coastal/remote islands. BC is considered to be inert and chemical inactive, so it is governed solely by physical processes and a good indicator of long-range transport. The analysis of BC can help identify regions with large continental influence.

451

3.2.1 Comparison with research cruise measurements

Figure 4a shows the observed and simulated daily BC concentrations along the cruise track during the spring campaign. An obvious spatial gradient was found for BC concentration, which was characterized by apparent higher concentrations of 0.5~4.2 μg m^{-3} over the marginal seas of China (the Yellow Sea and East China Sea, 18~19 March and 21~22 April) and very low concentrations of <0.2 μg m^{-3} over open oceans (during most of the measurement days). It is interesting to note that an observed BC peak occurred on 21 March, which could be attributed to the long-range transport of biomass burning plumes from northeast Asia (Luo et al., 2016; 2018). The model generally reproduced the spatial and temporal variations of BC concentration during the campaign period; however, the BC peak on 21 March was missed by the model simulation. Uncertainties in biomass burning emission could be responsible for such model bias. On average, the measured and simulated BC concentrations during this campaign onboard the Dongfanghong II cruise were 0.49 μg m^{-3} and 0.55 μg m^{-3}, respectively, with the R and NMB of 0.87 and 13% (Table 3).

Figure 4b shows the daily mean OC concentrations from observation and model simulation for the same cruise. In general, the observed OC exhibited a similar spatial distribution and temporal variation to that of BC, with higher concentrations over the marginal seas and relatively lower concentrations over open oceans. The model generally captured the spatial-temporal features along the cruise track. Like BC, the observed OC concentrations were high on 21 and 25~26 March mainly due to the continental outflow of biomass burning emissions from northeast Asia, and the model largely underpredict the high OC observation in these days. It is noteworthy that two OC peaks appeared on 10 and 12 April when the ship was over the open ocean east of Japan (the ship location was around 33.5°N, 146.0°E on 10 April and around 36.5°N, 145.0°E on 12 April, approximately 400~500 km to the east of Japan), whereas the elevation of BC concentration was not evident. Because BC and OC are often originated from the same anthropogenic and biomass sources, the inconsistency in daily variation between BC and OC in these areas implied a potential influence of marine sources rather than that from anthropogenic and biomass burning emissions. Coincidentally, during these days, daily Chl-a concentrations over the oceanic areas east of Japan (the region of 35°N to 43°N and 140.0°E to 150.0°E, north to the ship location) reached as high as 45 mg m^{-3}, as a comparison, the monthly mean Chl-a concentration in April over the same region was in a range of 2 to 14 mg m^{-3}. The apparent

481 higher Chl-a concentration during these days could induce changes in marine primary organic

482 emissions. On 10 April, the wind direction in the vicinity of the cruise was mainly southwesterly,

483 backward trajectory (figure not shown) indicates that air parcels travelled over low Chl-A regions to

484 the southwest of the cruise, implying a small effect of MOA. On this day, the fraction of land-OC (OC

485 originated from continental sources) in total OC was 68%, which was larger than that of marine

486 organic carbon (marine-OC) (32%) as shown in Figure 4b. On 12 April, northwesterly winds prevailed

487 over the cruise region, with backward air trajectory traveling over strong Chl-A regions to the

488 northeast of Japan (figure not shown), marine-OC aerosols produced from the bloom regions could be

489 blown to the southeast where ship located, leading to the elevation of OC concentrations (Figure 4b).

490 Marine-OC (percentage contribution of 74%) dominated over land-OC (26%) in the total OC

491 concentration on this day. The model improves OC simulation on 10 and 12 April when considering

492 marine organic aerosols (marine-OC in Figure 4b). However, it should be acknowledged that the

493 model appears to generally overpredict OC concentrations during 5~16 April over the ocean southeast

494 of Japan, especially on 5~6, 11 and 13 April. The high model biases could be due to potential

495 overpredictions for either land-source OC or marine-source OC. The cruise campaign average OC

496 concentration was 1.2 μg m^{-3} from observation and 1.1 μg m^{-3} from simulation, with the R and NMB

497 of 0.66 and -5%, respectively (Table 3). For the coastal/marginal sea areas (cruising time on 18 to 20

498 March and 20 to 22 April), the mean observed and simulated OC concentrations were 3.1 μg m^{-3} and

499 3.0 μg m^{-3}, respectively. For open sea areas (cruising time from 21 March to 19 April), the observed

500 and simulated OC concentrations were 0.69 μg m^{-3} and 0.65 μg m^{-3}, respectively. The inclusion of

501 marine-OC (including both primary and secondary OC) reduced the model bias from -33% to -5%

502 along the cruise. The average contribution of marine-OC to the total OC mass in the marine

503 atmosphere was approximately 29% along the cruise, with lower contributions of 11~27% over the

504 marginal seas of China (18~19 March and 21~22 April) and higher contributions of 32~74% over the

505 open oceans (5~18 April) (Figure 4b), demonstrating an increasing importance of marine organic

506 aerosols to total OC mass from the marginal seas to remote open oceans.

507   Shown in Figure 4c is OC samples collected onboard the KEXUE-1 Research Vessel over the

508 East China Sea during the early summer campaign and the corresponding model results along the

509 cruise track. There were four OC peaks observed during the campaign, with three occurring over the

510 northern parts of the East China Sea (on 20 May, 26~29 May, and 1~5 June) and one over the southern

part of the East China Sea on 22 May. The model reproduced the OC variation quite well during most of the cruise track, capturing the three OC peaks over the northern parts of the East China Sea although low biases occurred for the first peak (over the area of 27.5°N to 30.0°N and 121.6°E to 121.9°E). The model missed the second OC peak on 22 May over the southern part of the East China Sea (over the area of 22°N to 23°N and 121.5°E to 122.2°E). Kang et al. (2018) proposed that this peak was seriously affected by biogenic and biomass burning emissions from Southeast Asia (Philippines) because the OC concentrations from 21 to 25 May were characterized by high abundance of sesquiterpene-derived SOA which was mainly originated from terrestrial photosynthetic vegetation (e.g. trees and plants). Uncertainties in emission inventories, such as missing some biogenic sources (e.g. fungal spores, Fröhlich-Nowoisky et al. 2016) could be partly responsible to the model biases. In addition, some regions of Southeast Asia (e.g. Philippines) were not included in the study domain, instead, their influence on the study domain was represented by chemical boundary conditions from MOZART simulation, so, the uncertainties in chemical boundary conditions may also contributed to such biases. At the time of the third (25°N to 26°N and 118.8°E to 121.7°E) and fourth (28°N to 28.7°N and 119.6°E to 122.7°E) OC peaks, the ship was close to the shore and predominately affected by continental sources (such as anthropogenic and biomass burning emissions), the model captured the peaks quite well in terms of both temporal variation and magnitude. On average, the observed and simulated OC concentrations from the KEXUE-1 cruise were 4.3 $\mu g\ m^{-3}$ and 3.7 $\mu g\ m^{-3}$, respectively, with R and NMB of 0.75 and -13% (Table 3). The inclusion of marine-OC reduced the NMB from -19% to -13%. Along the cruise track, marine-OC was estimated to account for 6% (1~60%) of the total OC mass on average, with lower contribution over the seas close to the continent (1~9%) and higher contribution over the seas far from the continent (7~60%). During the KEXUE-1 cruise campaign, the contribution of marine-OC to total OC mass was obviously lower than that during the spring campaign conducted by the Dongfanghong II, because this cruise over the marginal seas of China was more affected by continental outflow of anthropogenic and biomass emissions compared with that mainly over the open oceans.

3.2.2 Comparison with measurements at island and coastal sites

Figure S1 shows the modeled BC is generally consistent with observations at island sites (Huaniao, Fukue, Okinawa, Chichijima) in terms of both spatial distribution and seasonal variation,

541 indicating a good skill of RIEMS-Chem in representing the physical processes and long-rang transport

542 of carbonaceous aerosols over the western Pacific.

543   OC observations are limited in the western Pacific Ocean. We collected observations at islands

544 from previous publications (Boreddy et al., 2018; Kunwar and Kawamura, 2014; Wang F. W. et al.,

545 2015) for model comparison. Figure 5 shows the model simulated and observed seasonal/monthly

546 mean OC concentrations at the three islands. It should be kept in mind that the observations are

547 averages of different years. At Huaniao Island (Figure 5a), a distinct seasonality of OC observation

548 was shown, with the highest OC concentration of 4.7 μg m^{-3} in DJF, followed by 3.7 μg m^{-3} in MAM

549 and 3.8 μg m^{-3} in SON, and the minimum of 1.1 μg m^{-3} in JJA (Table 4). It was encouraging that

550 RIEMS-Chem reproduced the OC seasonality at Huaniao Island quite well (Figure 5a), despite the

551 different years between simulation and observation. The simulated OC was also divided into land-OC

552 and marine-OC to quantify the relative contribution of these sources to total OC mass. The simulated

553 annual mean OC concentration was 3.2 μg m^{-3}, in which 2.6 μg m^{-3} (81%) was contributed by

554 land-OC and 0.6 μg m^{-3} (19%) by marine-OC (Table 4). The simulation was very close to the

555 observation of 3.3 μg m^{-3} (Table 4). It was striking that the inclusion of marine-OC obviously

556 improved the model performance, reducing the NMB from -21% to -3%, although the improvement of

557 prediction for SOA from land source may also reduce the model bias at Huaniao island. It was

558 noteworthy that marine-OC exhibited the maximum value in MAM and the minimum value in JJA.

559 The higher Chl-a concentration over the East China Sea in MAM might be responsible for the

560 maximum at Huaniao Island (Figure 7h and Table 7), whereas the lowest sea salt emission flux could

561 result in the minimum in summer (Table 7). In terms of seasonal mean, marine-OC accounted for 12%,

562 22%, 19%, and 23% of the total OC concentration in DJF, MAM, JJA, and SON, respectively, with an

563 annual mean contribution of 19% at Huaniao Island. The lowest relative contribution (12%) of

564 marine-OC in winter was attributed to the maximum anthropogenic OC emissions in eastern China in

565 this season.

566   At Okinawa (Figure 5b), the observed total OC showed the maximum in MAM, followed by that

567 in JJA, and the lower ones in DJF and SON during October 2009-2010. Figures 5a and 5b also show

568 that the seasonal cycling of OC concentration at Okinawa (Figure 5b) differed a lot from that at

569 Huaniao Island (Figure 5a). The high OC concentration in summer at Okinawa could be attributed to

570 higher SOA produced by local biogenic VOC emissions (Kunwar and Kawamura, 2014). The model

571 generally reproduced the seasonal variation of OC except that it predicted lower OC level in summer,

572 which could be due to the exclusion of local biogenic VOC emissions in the CAMS-GLOB-BIO

573 emission inventory. In terms of annual average, the observed OC concentration was 1.8 μg m^{-3}, larger

574 than the simulations of 1.3 μg m^{-3} from the FULL case including marine-OC and of 1.1 μg m^{-3} from

575 the case excluding marine organic emissions (Table 4). The inclusion of marine organic emissions

576 improved OC simulation at Okinawa, reducing the NMB from -39% to -28%. It was estimated that

577 marine-OC accounted for 18%, 17%, 10%, and 18% of total OC mass concentration at Okinawa in

578 DJF, MAM, JJA, and SON, respectively, with an annual mean contribution of 17%. The relatively

579 smaller contribution of marine-OC to the total OC mass at Okinawa than that at Huaniao Island (19%)

580 could be attributed to the higher Chl-a concentration and MPOA emission flux in the marginal seas of

581 China than those over remote western Pacific south of Japan (Figure 7).

582   Long-term average (2001-2012) of monthly mean OC concentrations at Chichijima Island

583 reported by Boreddy et al. (2018) and the simulated monthly mean OC concentration in 2014 were

584 shown in Figure 5c. The observations show higher OC levels from January to March mainly due to

585 continental outflows. It was noticed that the simulated OC levels in April-May were apparently higher

586 than observations, which could be associated with different time periods between observation and

587 simulation, and with potentially stronger continental outflows and bloom in spring 2014 than those of

588 ten-year averages. OC observations were relatively lower in summer and autumn due to the

589 dominance of high-pressure system and pristine ocean air mass over the western Pacific (Figure 9d

590 and 9e). The model tended to predict lower OC level in summer and autumn (Figure 5c). Boreddy et

591 al. (2018) indicated that in summer and autumn, OC at Chichijima was often influenced by long-range

592 transport of biomass burning plumes from Southeast Asia, which was not well represented in the

593 model (using chemical boundary conditions from MOZART-4 instead) and led to low model bias. On

594 average, the annual mean OC concentration was 0.76 μg m^{-3} from observation, and 0.78 μg m^{-3} from

595 the FULL case, and 0.65 μg m^{-3} without considering marine-OC (Table 5). The inclusion of marine

596 organic emissions reduced the annual mean NMB from -13% to 3% and enhanced the correlation

597 coefficient from 0.56 to 0.6 at this site. The apparent better simulation from the FULL case indicated

598 the necessity of inclusion of marine organic emissions for simulating OC over the remote oceans of

599 the western Pacific. Both observation and model simulation revealed higher seasonal mean OC

600 concentrations in MAM (observed: 0.83 μg m^{-3}, simulated: 0.91 μg m^{-3}) and DJF (observed: 0.9 μg

m^{-3}, simulated: 1.2 μg m^{-3}) when the measurement site was frequently influenced by continental outflows, whereas lower concentrations in JJA (observed: 0.65 μg m^{-3}, simulated: 0.47 μg m^{-3}) and SON (observed: 0.66 μg m^{-3}, simulated: 0.57 μg m^{-3}) when clean maritime air masses or biomass burning plumes from Southeast Asia (e.g. Philippine) influenced this region. The highest marine-OC concentration was 0.19 μg m^{-3} in MAM, followed by 0.16 μg m^{-3} in DJF and 0.11 μg m^{-3} in SON, and the lowest one of 0.05 μg m^{-3} in JJA. However, the percentage contribution of marine-OC to the total OC mass was estimated to be largest in SON (20%), followed by 18% in DJF, 16% in MAM, and lowest in JJA (10%), with an annual mean contribution of 16% (Table 5). The largest contribution in SON was associated with the relatively lower total OC concentration as shown in Figure 5c. The relative contribution from marine-OC to total OC at Chichijima Island resembled that at Okinawa in terms of annual and season averages.

The above comparison against a variety of OC observations demonstrated a generally good skill of RIEMS-Chem in simulating OC over the western Pacific in terms of seasonal variation and magnitude. The model results from the FULL case indicated that including marine organic emissions improved OC simulation over the western Pacific Ocean.

3.2.3 SOA over the western Pacific

Recently, Guo et al. (2020) reported SOA observations in the marine atmosphere from the marginal seas of east China to the northwest Pacific Ocean. The measurements were conducted on three research cruises in the spring and early summer of 2014 and in the spring of 2017. Total suspended particulate (TSP) samples were collected from 19 March to 21 April 2014 over the northwestern Pacific Ocean (NWPO), from 30 April to 17 May 2014 over the Yellow and Bohai seas (YBS), and from 29 March to 4 May 2017 over the South China Sea (SCS). SOA concentration was derived by using a tracer-based method. The measured SOA concentrations were 467±384 ng m^{-3} over the YBS, 617±649 ng m^{-3} over the SCS, and 155±236 ng m^{-3} over the NWPO, respectively. The model simulated period and regional mean SOA concentrations were 664 ng m^{-3} over the YBS, 466 ng m^{-3} over the SCS, and 157 ng m^{-3} over the NWPO, which were generally consistent with the above observations, although the study periods are not exactly the same. Guo et al. (2020) also presents the tracer-based estimations of isoprene and monoterpene derived SOA in the air masses from ocean (assuming marine sources), which were 1.7 ng m^{-3} and 0.3 ng m^{-3}, respectively, over the western

Pacific to the southeast of Japan, whereas the modeled SOA concentrations produced from marine isoprene and monoterpene emissions along the cruise track were 1.6 ng m^{-3} and 0.28 ng m^{-3}, respectively, generally agreeing with the tracer-estimation. However, it should be mentioned that there could be uncertainties in such comparison. First, the isoprene- and monoterpene-derived SOA tracers in the air masses categorized as marine sources by Guo et al (2020) might include SOA tracers from terrestrial isoprene and monoterpene under the prevailing northwesterly winds in spring, which could bias the estimation high; second, the measured tracer could just comprise a part of total SOA tracers, which might bias the estimation low. Despite these uncertainties, the cruise measured SOA concentration derived from marine isoprene and monoterpene was approximately several ng m^{-3} over the western Pacific, and it can reach approximately 10 ng m^{-3} even through dividing by a mass fraction of tracer compound to yield the concentration of total SOA tracers. It was noteworthy that both observation and model simulation exhibited a decreasing SOA concentration from marginal seas of China to remote oceanic areas. In all, the model reproduced the SOA levels in the marine atmosphere of the western Pacific Ocean reasonably well.

The comparison of the magnitudes between SOA and OA mass (1.4 times OC mass) concentrations shown above indicates that SOA concentration was approximately 1~2 orders of magnitude lower than OA over the western Pacific. Previous observation studies using the tracer-based approach also indicated that the percentage contribution of SOA to OA was quite low over some marine areas (Fu et al., 2011; Hu et al., 2013; Bikkina et al., 2014; Zhu et al., 2016). For example, at Okinawa island, even considering all biogenic sources (including isoprene, monoterpene, and sesquiterpene of both terrestrial and oceanic origins), the measured concentration of total biogenic-SOA tracers was still less than 100 ng m^{-3}, with majority of SOA tracers from local terrestrial biogenic emissions (Zhu et al., 2016). The above studies suggested that primary organic aerosols were more important in remote marine atmosphere.

3.3 Aerosol optical depth

Figure 6 shows the temporal variations of the observed and simulated monthly mean AOD at the 7 AERONET sites. In general, RIEMS-Chem simulated the monthly mean AOD reasonably well in terms of magnitude and monthly variation at almost all sites, although some biases occurred during some months, such as the overpredictions in August at Fukuoka and in April at EPA-NCU, and the

underprediction in July at Yonsei University. For the sites in the northern oceanic areas (Ussuriysk, Yonsei_University, Gwangju_GIST, and Fukuoka, Figure 6a~6d), both observations and simulations generally exhibited higher AOD values in summer (JJA), moderately high AOD values from late winter (JF) to spring (MAM), and relatively lower AOD values in autumn (SON). The simulated higher inorganic aerosol concentrations in summer and late spring months could be responsible for the higher AOD values in these regions. Besides, the higher relative humidity in summer due to the predominant influence of maritime air masses also contributed to the maximum AOD values during summer months (JJA) at these sites. On the other hand, for the sites in the southern oceanic areas (EPA-NCU and Chen-Kung_Univ, Figure 6e and 6f), the monthly mean AOD was apparently higher from March to April and remained low levels during the rest months. The above AOD peaks in spring could be attributed to the continental outflows of biomass burning plumes originated from Southeast Asia, which were most active in springtime in those regions (Hsiao et al., 2017; Tao et al., 2020). Table 6 shows the performance statistics for hourly AOD at these AERONET sites. The overall annual mean AOD for the 7 sites was 0.34 from model simulation, which was very close to the observation of 0.36, with the NMB of -6% and the overall correlation coefficient of 0.54 (0.40~0.67). The statistics indicate that the model was able to reproduce aerosol optical properties over the coastal regions and islands around the western Pacific Ocean. Contributions of MOA, sea salt, and non-oceanic aerosols (anthropogenic and other natural aerosols from the Asian continent) to total AOD are also shown in Figure 6. It clearly shows the predominant contribution to AOD from non-oceanic aerosols at all sites. It is also noticed that AOD induced by sea salt is generally larger than that by MOA, but they are comparable at the Chen-Kung Univ and EPA-NCU sites in spring (Figure 6f and 6g).

The model simulated annual mean AOD at 550 nm are also compared with the VIIRS retrievals (Figure S2), which indicates the model is generally capable of reproducing AOD distribution and magnitude in the study domain. The generally high model bias over the western Pacific could be attributed to potential overpredictions of inorganic aerosol concentration and relative humidity. AOD reflects the column integrated extinction coefficient due to all aerosols.

At the AERONET sites, the model simulated annual mean percentage contribution of MOA to AOD varied from 1.4% to 3.2% with an overall average of 1.9%. For the oceanic VIIRS region, the mean contribution of MOA to AOD was approximately 2%.

691   4 Model results

692   4.1 Marine primary organic and isoprene emissions

693   Figure 7 shows the estimated annual and seasonal mean MPOA emission rates over the western

694   Pacific of East Asia. The MPOA emission mainly occurred over two hotspot regions: the marginal

695   seas of China including the East China Sea, the Yellow Sea, and the Bohai Sea (EYB, 27°N~40°N,

696   115°E~123°E, denoted in Figure 7a) and the northern parts of the western Pacific northeast of Japan

697   (NWP, 35°N~54°N, 140°E~160°E, denoted in Figure 7a), with annual mean emission rates varying

698   from 0.9×10^{-2} µg m^{-2} s^{-1} to 1.8×10^{-2} µg m^{-2} s^{-1}. In SON, high MPOA emission occurred in both the

699   EYB and NWP regions, with the maximum up to 3.5×10^{-2} µg m^{-2} s^{-1} in the NWP (Figure 7e),

700   whereas MPOA emission was very low over the EYB in JJA (Figure 7d). The maximum seasonal

701   mean emission rate of MPOA approached 3.6×10^{-2} µg m^{-2} s^{-1} over the Yellow Sea in DJF (Figure 7b),

702   which was approximately 1/10 of the annual mean anthropogenic POA emission rate in north China

703   (on the order of $1.0 \sim 3.0 \times 10^{-1}$ µg m^{-2} s^{-1}). Table 7 presents the seasonal and annual averages of MPOA

704   emission averaged over the western Pacific and the EYB and NWP regions (note they are oceanic

705   averages with land grids excluded). In terms of oceanic average of the western Pacific, the mean

706   MPOA emission generally exhibited the largest emission rate in SON (0.2×10^{-2} µg m^{-3} s^{-1}),

707   moderately high emission rates in DJF (0.18×10^{-2} µg m^{-2} s^{-1}) and MAM (0.17×10^{-2} µg m^{-2} s^{-1}), and the

708   lowest one in JJA (0.08×10^{-2} µg m^{-2} s^{-1}), with an annual average of 0.16×10^{-2} µg m^{-2} s^{-1} (Table 7). It is

709   interesting to note that the seasonal variation of MPOA emission was not consistent with that of Chl-a

710   concentration, which exhibited higher values in SON and JJA and the lowest one in DJF (Table 7).

711   This is because MPOA emission rate is determined by the combined effect of Chl-a concentration and

712   sea salt emission flux, and sea salt flux is mainly controlled by surface wind speed according to the

713   scheme of Gong (2003). In terms of seasonal and domain average over the western Pacific, the

714   maximum Chl-a concentration and the second largest sea salt emission flux in SON led to the largest

715   MPOA emission in autumn (Table 7). However, although Chl-a concentration was also high in JJA

716   (1.07 mg m^{-3}, Table 7), the sea salt flux was minimum in JJA (0.14 µg m^{-2} s^{-1}, Table 7) due to the

717   weakest wind speed (3.0 m s^{-1}, Table 9), resulting in the lowest MPOA emission in summer (Table 7).

718   Although the sea salt emission flux reached the maximum in DJF (Table 7) due to the largest wind

719   speed in this season (Table 9), the winter Chl-a concentration was lowest, leading to a moderate

720   MPOA emission in winter (Table 7), in a similar magnitude to that in spring when moderately high

721 Chl-a concentration and relatively low sea salt flux occurred. In all, the MPOA emission rate over the

722 western Pacific exhibited an apparent seasonality of SON > DJF ≈ MAM > JJA.

723   For the EYB region, the maximum MPOA emission occurred in winter (DJF) (Figure 7b and

724 Table 7) with a seasonal and domain average of 1.2×10^{-2} μg m^{-2} s^{-1}, which was 10 times larger than

725 the minimum of 0.12×10^{-2} μg m^{-2} s^{-1} in summer (JJA) (Figure 7d and Table 7). Although Chl-a

726 concentrations were similar between DJF and JJA, the sea salt flux in DJF was approximately 9 times

727 that in JJA (Table 7). So, the seasonality of MPOA emission in the EYB region was mainly

728 determined by that of sea salt emission flux due to the weak seasonal variation of Chl-a concentration.

729 Differently, in the NWP region, MPOA emission exhibited the maximum value in SON, followed by

730 those in MAM and DJF, and the lowest ones in JJA (Table 7). It is interesting to note that although

731 both the Chl-a concentration and sea salt emission flux were slightly higher in MAM than those in

732 SON, the MPOA emission (related to both Chl-a concentration and sea salt emission) was higher in

733 SON, which could due to the slight negative correlation between Chl-a and sea salt emission in MAM,

734 but the slight positive one in SON. The MPOA emissions in winter and summer were in a similar level

735 in the NWP region, about 40% lower than that in autumn.

736   The distribution pattern of MPOA emission in the western Pacific from this study is similar to

737 those from previous model studies (Spracklen et al., 2008; Gantt et al., 2009; Huang et al., 2018), but

738 the magnitude of the simulated MPOA emission flux is larger than previous estimates. For example,

739 the annual mean MPOA emission rates over the western Pacific were estimated to vary from 0.1 to

740 approximately 12 ng m^{-2} s^{-1} in previous studies (Spracklen et al., 2008; Vignati et al., 2010; Gantt et

741 al., 2011; Long et al., 2011; Huang et al., 2018), whereas the estimates in this study ranged from 3 to

742 18 ng m^{-2} s^{-1} (Figure 7a). The larger marine POA emission estimated in this study could be attributed

743 to the application of the daily mean Chl-a concentration from satellite retrievals and of a finer model

744 grid resolution (60 km) compared with those in global models. On average, the annual MPOA

745 emission was estimated to be 0.78 Tg yr^{-1} over the western Pacific (with an ocean area of 1.6×10^{7} km^{2})

746 from this study. The regions of EYB and NWP comprised approximately 2% and 18% of the western

747 Pacific in terms of area, respectively, but they contributed 8% and 46% of the MPOA annual emission

748 (Tg y^{-1}). This study revealed that the EYB and NWP are important bloom regions, totally accounting

749 for more than half of the total MPOA emission over the western Pacific.

750   Table S3 presents the simulated marine isoprene emission fluxes from this study and the estimates

based on cruise observations over the western Pacific of East Asia from previous studies. Over the western North Pacific, the observed marine isoprene emission flux showed larger values in May (140 nmol m^{-2} day^{-1} from Matsunaga et al. (2002) and 143.8 nmol m^{-2} day^{-1} from Ooki et al., (2015)), a moderate value in August (55.6 nmol m^{-2} day^{-1} from Ooki et al., (2015)), and the lowest one in winter (21.4 nmol m^{-2} day^{-1} from Ooki et al., (2015)). The simulation from this study generally agreed with observation in terms of both seasonality and magnitude except for the low bias in May (85~89 nmol m^{-2} day^{-1} vs observation-based estimates of 140~143.8 nmol m^{-2} day^{-1}), which could be associated with the different years. According to equations (2) and (3) (in the supplement), both Chl-a concentration and incoming solar radiation determine marine biogenic VOCs emission, the larger isoprene flux in May was mainly due to the maximum Chl-a concentration in spring over the NWP region (Table 7). Over the marginal seas of China, Li J. L. et al. (2017; 2018) observed higher marine isoprene emission flux in July-August (161.5 nmol m^{-2} day^{-1}) than those in October-November (48.3 nmol m^{-2} day^{-1}) and May-June (36.1 nmol m^{-2} day^{-1}) during 2013-2014. The model results from this study show the similar seasonal variation and magnitude of isoprene flux, with corresponding mean values of 130 nmol m^{-2} day^{-1}, 48 nmol m^{-2} day^{-1}, and 35 nmol m^{-2} day^{-1} during the same periods of 2014, respectively. The apparently higher isoprene flux in July-August was mainly resulted from the strongest solar radiation in summer, although the Chl-a concentration was not highest in this season in the EYB region (Table 7). The domain-wide annual marine isoprene emission estimated over the western Pacific was 0.015 Tg yr^{-1} in this study.

4.2 Marine organic aerosols and their relative importance

Annual and seasonal mean near surface MOA concentrations, MSOA concentrations, and the percentage contributions of MOA to total OA mass in the study domain were shown in Figure 8. The spatial distributions of MOA concentrations (Figure 8a~8e) generally resembled those of MPOA emissions (Figure 7a~7e). It is remarkable that MPOA concentration (MOA minus MSOA) was approximately 1~2 orders of magnitude higher than MSOA concentration (with concentration of several ng m^{-3}) in the western Pacific (Figure 8a~8e vs Figure 8f~8j), indicating that MPOA constituted a dominant fraction of MOA, which will be discussed below. Figure 8a shows that high MOA concentrations mainly occurred over the EYB and NWP regions, with the annual and regional averages being 0.48 µg m^{-3} and 0.59 µg m^{-3}, respectively (Table 8), accounting for 13% (6~30%) and

781 42% (30~60%) of total OA mass in these two regions, respectively (Figure 8k and Table 8). The larger

782 MOA contribution over the NWP was attributed to the high MOA level and the relatively low total OA

783 level there. It is noticed that MOA even influenced the coastal areas of eastern China. The annual

784 mean MOA concentration decreased from approximately 0.5 μg m^{-3} in coastal areas to 0.1 μg m^{-3} in

785 the inland areas approximately 600 km away from the coastline (Figure 8a), accounting for

786 approximately 2% to 6% of the near-surface OA mass in the coastal regions (Figure 8k). The

787 maximum seasonal mean MOA concentration over the coastal areas of eastern China could be up to

788 0.6 μg m^{-3} to 0.8 μg m^{-3} in MAM (Figure 8c) and SON (Figure 8e). The domain and seasonal mean

789 MOA concentration over the western Pacific exhibited the maximum value in MAM (0.37 μg m^{-3}),

790 follow by that in SON (0.26 μg m^{-3}), and relatively lower concentrations in JJA (0.23 μg m^{-3}) and DJF

791 (0.21 μg m^{-3}) (Table 8). It was noteworthy that the seasonality of MOA concentration was different

792 from that of MPOA emission, which could be attributed to the influence of different meteorological

793 conditions and physical processes. In the western Pacific, although MPOA emission peaked in SON

794 (Table 7), MOA concentration peaked in MAM (Table 8). It is noticed that precipitation was lowest

795 and wind speed was low in MAM (Figure 9c and 9h, Table 9), leading to a smaller dry deposition

796 velocity (Zhang et al. 2001) and the weakest wet scavenging, both favored accumulation of MOA and

797 thus resulted in the highest MOA level in spring. On the contrary, due to the maximum wind speed

798 and relatively more precipitation in DJF (Figure 9b and 9g, Table 9), the mean MOA concentration

799 was lowest in winter.

800 For the EYB region, northwesterly winds prevailed In DJF and SON and turned to northeasterly

801 winds over marginal seas of southeast China (Figure 9b and 9e), which transported MOA from the

802 major MPOA source region (EYB) to the northern part of the South China Sea (Figure 8b and 8e). As

803 wind speed over the EYB was low in MAM and JJA (Figure 9c and 9d, Table 9), MOA was mainly

804 restricted within this region (Figure 8c and 8d). In terms of seasonal average, MOA concentration

805 experienced its maximum in MAM, followed by those in DJF and SON, and the minimum in JJA

806 (Figure 8b~8e). The seasonal and regional mean MOA concentrations over the EYB were 0.62 μg m^{-3},

807 0.54 μg m^{-3}, 0.52 μg m^{-3}, and 0.22 μg m^{-3} for MAM, DJF, SON, and JJA, respectively (Table 8). The

808 different seasonality between MOA concentration (Table 8) and MPOA emission (Table 7) in the EYB

809 region could also be mainly attributed to meteorological conditions. The MPOA emission was

810 relatively low in MAM (Table 7), but the second lowest wind speed and less precipitation (Table 9)

favored aerosol accumulation, resulting in the highest MOA concentration in spring (Table 8). The minimum MPOA emission and the maximum precipitation in JJA led to the minimum MOA concentration in summer. Although MPOA emission was largest in SON and DJF (Table 7), the maximum wind speeds (Table 9) led to stronger dry deposition of aerosols and thus a moderate MOA concentration in the two seasons (Table 8).

MOA concentration over the NWP region exhibited apparent higher concentrations in MAM and JJA than those in SON and DJF (Figure 8b~8e), with the regional and seasonal averages reaching 0.81 μg m^{-3} in MAM, 0.80 μg m^{-3} in JJA, 0.52 μg m^{-3} in SON, and 0.23 μg m^{-3} in DJF, respectively (Table 8). Using GEOS-Chem with a different marine organic aerosol emission scheme, Spracklen et al. (2008) also showed that in the North Atlantic along the similar latitude bands to the NWP (~35°N to ~55°N), both observation and simulation exhibited higher OC concentrations in summer and spring than in the other seasons at the Azores Island and Mace Head Island. The strong seasonality of MOA over the NWP was also attributed to the combined effects of MPOA emission, wind speed, and precipitation. In MAM, the high MOA concentration over the NWP was mainly due to the large MPOA emission (Figure 7c and Table 7), which was just smaller than that in SON, and partly due to the relatively weak dry deposition and wet scavenging caused by moderate wind speed and precipitation in this season (Table 9). In JJA, although the MPOA emission was small, the lowest wind speed and precipitation in JJA over the NWP (2.5 m s^{-1} and 3.7 cm grid^{-1} month^{-1}, Table 9) led to the weakest dry deposition and wet scavenging of particles in summer, resulting in a long residence time of MOA and consequently the high MOA concentration in summer over the NWP. In SON, although the MPOA emission was largest over the NWP (Table 7), the mean wind speed was high over the northern part of the NWP (Figure 9e) where MPOA emission mainly occurred (Figure 7e), leading to strong dilution of MOA particles in autumn. Furthermore, SON had the secondly largest precipitation over the NWP (Table 9), which caused strong wet scavenging of particles and also contributed to the relatively low MOA level. In DJF, the wind speed was largest, about 2 times those in the other seasons, and the precipitation was also the maximum (Table 9, Figure 9b and 9g), leading to the lowest MOA concentration in winter over the NWP (Figure 8b and Table 8).

As shown in Figures 8k~8o, MOA generally accounted for approximately 30% to over 60% of total OA concentration over the remote oceans of high (>35°N) and low (<25°N) latitudes within the model domain. The large MOA/OA ratios over the remote oceans of high latitude (including NWP)

could be attributed to the high MOA concentration due to large marine emissions there; whereas, the large MOA/OA ratios over the subtropical oceans of low latitude were mainly due to the low total OA level (small denominator). Averaged over the NWP region, the annual mean MOA/OA ratio was 42%, with higher contributions in MAM (52%) and SON (48%) and lower ones in DJF (36%) and JJA (32%) (Table 8). Although MOA concentration over the NWP was secondly highest in JJA, its contribution was small because OA transported from land sources also subject to weak dry deposition and wet scavenging, which led to higher OA level and lower MOA/OA ratio. Over the EYB region, MOA accounted for approximately 6% to 30% of the total OA in terms of annual mean (Figures 8k). In terms of annual and regional average, the MOA/OA ratio was 13%, with higher ratios in SON (18%) and MAM (15%), a moderate one in DJF (11%), and the lowest one in JJA (6%) (Table 8), similar to the seasonality over the NWP. For the oceanic areas, the domain and annual mean MOA/OA ratio was 26%, indicating an important contribution of MOA to airborne OA over the western Pacific. It was found that the importance of MOA in total OA increased as the distance to the East Asian continent increased over the western Pacific. It is also interesting to note that MOA even accounted for approximately 2~6% of the annual mean OA mass over portions of southeast China (Figures 8k), and such contribution could be as high as 8~10% in the coastal areas in SON (Figures 8o) and MAM (Figures 8m).

In all, both the MOA concentration and the MOA contribution to total OA were lowest in summer (JJA) in the EYB region, which was mainly due to the much smaller MPOA emission in this season. However, in the NWP region, although the MPOA emission was also lowest in summer, MOA concentration in summer was in a same level as that in spring, and larger than those in the other seasons, because dry deposition velocity and precipitation were lowest in summer, which favored aerosol accumulation and a high level of MOA.

SOA produced by marine biogenic VOCs (isoprene and terpene) was on the order of 10^{-2}~10^{-3} μg m^{-3} (Figure 8f~8j), which was much lower than the MPOA concentration. The spatial distribution of MSOA exhibited high concentrations over the EYB and NWP regions in terms of annual mean, with values up to 6 ng m^{-3} (approximately 0.5% of MOA concentration) over these two regions (Figure 8f). MSOA concentration exhibited the maximum in JJA, with seasonal mean values of 7 ng m^{-3} to 11 ng m^{-3} extending from the marginal seas of China (EYB) to remote western North Pacific (NWP) (Figure 8i). MSOA distribution in MAM was similar to that in JJA but with lower mean concentrations (4~7

871   ng m^{-3}) over the EYB and NWP regions (Figure 8h). In SON (Figure 8j), MSOA concentrations were

872   2~4 ng m^{-3} in the above two regions. In DJF (Figure 8g), MSOA concentration was lowest, with

873   values of 0.4~2 ng m^{-3} over the marginal seas of China and the southern parts of the model domain.

874   The maximum seasonal mean MSOA concentration was up to 14 ng m^{-3} over oceanic areas of the

875   EYB to NWP regions in JJA, and the maximum daily mean MSOA value exceeded 28 ng m^{-3} on some

876   days, e.g. June 6~7 (figure not shown). Table 8 shows the domain and seasonal/annual averages of

877   MSOA over the oceanic regions of concern. The annual mean MSOA concentrations were 2.2 ng m^{-3},

878   4.1 ng m^{-3} and 3.8 ng m^{-3} averaged over the western Pacific, the EYB and NWP regions. It is striking

879   that the domain average MSOA concentration consistently exhibited a distinct seasonality, with the

880   maximum in summer and the minimum in winter throughout all the oceanic regions of the western

881   Pacific, which was resulted from the combined effects of isoprene emission flux and meteorological

882   conditions. The domain average MSOA concentrations reached the maximums of 3.9 ng m^{-3}, 7.5 ng

883   m^{-3}, and 8.3 ng m^{-3}, respectively, over the western Pacific, the EYB and NWP regions in JJA. The

884   seasonality of MSOA concentration over the western Pacific is similar to the simulation result from

885   Myriokefalitakis et al. (2010). According to Table 8, the annual mean fraction of MSOA in MOA was

886   estimated to be 0.8%, 0.9% and 0.6%, over the western Pacific, the EYB and NWP regions,

887   respectively. The maximum and minimum fractions of MSOA in MOA averaged over the western

888   Pacific occurred in JJA (1.7%) and DJF (0.3%), respectively, with the maximum regional and

889   seasonal average MSOA fraction up to 3.4% in summer over the EYB region. Based on the

890   GEOS-Chem model simulation, Arnold et al. (2009) indicated that SOA produced by marine isoprene

891   contributed only a very small fraction (0.01~1.4%) of the observed organic aerosol mass at remote

892   marine sites (Amsterdam Island in southern Indian Ocean, Azores and Mace Head islands in northern

893   Atlantic Ocean). In a global model simulation from Myriokefalitakis et al. (2010), the annual mean

894   marine isoprene and monoterpene derived SOA concentrations were approximately 0.4~1 ng m^{-3}

895   (accounting for ~0.4% of marine OA) over the western Pacific. Meskhidze et al. (2011) illustrated the

896   marine SOA from phytoplankton-derived isoprene and monoterpenes contributed <10% of surface

897   OM concentration of marine source in most areas of the western Pacific.

898

899   4.3 Direct radiative effect due to MOA

900   In this section, the direct radiative effect (DRE) due to MOA (DRE$_{MOA}$) over the western Pacific

of East Asia was estimated and analyzed. DRE is defined as the difference in net shortwave radiation flux at TOA (or at the surface) induced by aerosols. The DRE of MOA is derived by the difference between two radiation calls with aerosol optical properties (aerosol optical depth, single scattering albedo, asymmetry factor) due to total aerosols including sea spray (sea salt+MOA), anthropogenic aerosols and other natural aerosols (mineral dust, SOA from vegetation emitted VOCs) in this model and with those due to total aerosols but MOA (i.e., call two times in the radiation module in the same simulation), reflecting an instantaneous change in shortwave radiation fluxes induced by MOA. DRE of other aerosol components is estimated by using the same method. The direct (indirect) radiative effect is calculated with the following general equation in this study:

$$D(I)RE_{ai}=(F\downarrow-F\uparrow)_{all\ aerosols}-(F\downarrow-F\uparrow)_{all\ aerosols\ but\ ai}$$

Here $F\downarrow$ and $F\uparrow$ represents incoming and outgoing shortwave radiation fluxes, respectively, a_i denotes a specific aerosol component, e.g., MOA.

Figures 10a to 10e show the annual and seasonal mean DRE_{MOA} at TOA under all-sky condition. MOA induced negative DRE over the entire western Pacific. Consistent with the spatial distribution of MOA concentration, the maximum DRE_{MOA} up to -0.9 W m^{-2} occurred over the NWP region (Figure 10a), with statistical significance at the 99% confidence level over limited areas of NWP (note the areas of statistical significance at the 95% confidence level is larger). Over the EYB region, the other hotspot of MOA mass concentration, the DRE_{MOA} was weaker, with an annual mean DRE_{MOA} of ~ -0.4 W m^{-2} (Figure 10a). In terms of domain average, the annual mean DRE_{MOA} was estimated to be -0.27 W m^{-2} over the western Pacific, smaller than that over the NWP (-0.5 W m^{-2}) but similar to that over the EYB (-0.33 W m^{-2}) (Table 10). The weaker DRE_{MOA} over the EYB than that over the NWP could be attributed to both the lower MOA concentration (Table 8) and lower relative humidity (73% vs 83%, Table 9) because low relative humidity is unfavorable for hygroscopic growth of MOA, leading to a smaller light extinction coefficient and thus weaker DRE. The mean DRE_{MOA} over the western Pacific was largest in spring (-0.38 W m^{-2}) and lowest in winter (-0.18 W m^{-2}) (Table 10), consistent with the seasonality of MOA concentration.

In the NWP region, MOA induced the largest DRE up to -2.0 W m^{-2} to the northeast of Japan in MAM (Figure 10c) and followed by that in JJA (up to -1.5 W m^{-2}) (Figure 10d) with statistical significance at the 99% confidence level, mainly due to higher MOA concentrations in the two seasons. The DRE_{MOA} value was relatively low in SON (~ -0.7 W m^{-2}) (Figure 10e), and it was lowest

in DJF, with the maximum of just -0.4 W m^{-2} without statistical significance (Figure 10b) due to the lowest MOA concentration in winter (Table 8). The regional and seasonal means of DRE$_{MOA}$ over the NWP were estimated to be -0.76 W m^{-2}, -0.72 W m^{-2}, -0.32 W m^{-2}, and -0.21 W m^{-2} in MAM, JJA, SON, and DJF, respectively (Table 10). On the contrary, in the EYB region, DRE$_{MOA}$ exhibited a different seasonal trend from that over the NWP, exhibiting the largest DRE in SON (Figure 10e), moderate DREs in MAM (Figure 10c) and DJF (Figure 10b), and the lowest one in JJA (Figure 10d), with corresponding mean values of -0.38 W m^{-2}, -0.34 W m^{-2}, -0.32 W m^{-2}, and -0.26 W m^{-2}, respectively, for the four seasons (Table 10). The different seasonal variation of DRE in EYB and NWP could be mainly attributed to the different seasonality of MOA concentrations in these two regions.

It is of interest to estimate the relative importance of MOA in directly perturbing solar radiation compared with other types of aerosols over the western Pacific. Table 10 lists the simulated annual and seasonal mean DREs due to sea salt and anthropogenic aerosols over the western Pacific and the regions of NWP and EYB, respectively. It is noted that the annual mean DRE$_{MOA}$ was approximately one third of that due to sea salt and one order of magnitude lower than that due to anthropogenic aerosols on average over the western Pacific in this simulation. Over the EYB region, DRE$_{MOA}$ was almost negligible compared with that by anthropogenic aerosols due to the predominance of anthropogenic emissions near the continent, however, it is noteworthy that DRE$_{MOA}$ was comparable in magnitude to the DRE by sea salt, especially in springtime (-0.34 vs -0.36 W m^{-2} in MAM) when MOA concentration reached its maximum (Table 8). Over the remote oceans (NWP), DRE$_{MOA}$ was approximately 19% of the DRE by anthropogenic aerosols due to weakened influence of continental anthropogenic emissions over open oceans, and it was comparable in magnitude to the DRE by sea salt, especially in summertime (0.72 vs 0.79 W m^{-2}) when sea salt emission flux was lowest (Table 7). The annual and regional mean all-sky DRE$_{MOA}$ were approximately 10%, 5%, and 19% of the DREs due to anthropogenic aerosols over the western Pacific, the EYB, and NWP, respectively, and it was comparable in magnitude to the DREs by sea salt in the EYB and NWP regions.

It should be mentioned that due to the much smaller MSOA concentration than MPOA concentration, the above DRE$_{MOA}$ was dominantly contributed by MPOA, similar to the findings from previous studies (Arnold et al., 2009; Booge et al., 2016; Li et al., 2019). MPOA also dominated over MSOA in the following IRE estimation.

961

4.4 Indirect radiative effect due to MOA

The first indirect effect refers to that aerosol particles tend to increase cloud droplet number concentration, decrease cloud effective radius under stable cloud liquid water content, and thus modify cloud optical properties and radiation, which is also denoted as the indirect radiative effect (IRE) in this study. IRE due to marine organic aerosols (IRE_{MOA}) over the western Pacific of East Asia was explored in this section. The model is able to generally reproduce the major distribution features of annual mean cloud fraction and cloud optical depth in comparison with MODIS retrievals, which generally shows higher values from southeast China to the NWP region (Figure not shown). The first indirect radiative effect or IRE of MOA is estimated by the instantaneous difference in net shortwave radiation flux at TOA (or at the surface) between two radiation calls with cloud properties (cloud optical depth, cloud single scattering albedo, cloud asymmetry factor) due to total aerosols and with those due to total aerosols but MOA in one simulation. The lower bound of cloud droplet number concentration (N_c) is set to $10/cm^3$, which roughly represents N_c in liquid clouds in clean ocean conditions, according to satellite observations and global simulations. Hoose et al. (2009) pointed out that the choice of low bound of N_c may lead to uncertainties in IRE estimation.

Here, the calculation of IRE due to MOA (the sum of MPOA and MSOA) is called the base case (BASE), from which a series of sensitivity simulations are carried out below.

N_c due to aerosol activation is diagnosed by the A-G scheme, then the cloud effective radius r_e is calculated as a function of N_c and cloud liquid water content following the approach of Martin et al. (1994), and the cloud optical parameters (liquid cloud extinction optical depth, single scatter albedo, asymmetry factor etc.) are calculated by the scheme of Slingo et al. (1989), finally, shortwave radiation fluxes are calculated by the CCM3 radiation scheme (Kiehl et al., 1996).

The annual and seasonal mean IRE_{MOA} at TOA are shown in Figure 10f to 10j. IRE_{MOA} was negative in the entire domain, resulting from a series of changes in cloud properties induced by MOA, i.e., an increase in cloud droplet number concentration, a decrease in cloud droplet effective radius, an increase in cloud optical depth and cloud water path, and consequently more reflection of solar radiation at TOA. The model simulated cloud properties have been compared against satellite retrievals in spring 2014 in our previous study (Han et al., 2019), which indicated the model was able to reasonably reproduce the major features of cloud distribution. It is remarkable that IRE_{MOA} was

stronger than DRE_{MOA} over the western Pacific, with the maximum annual mean of IRE_{MOA} being approximately three times the maximum of DRE_{MOA}, and the positions of their maximum values were different. The annual mean IRE_{MOA} of $-0.9 \sim -2.5$ W m^{-2} distributed from southwest to northeast over wide areas of the western Pacific (Figure 10f) with statistical significance at the 99% level over most of the NWP region. It was evident that the strongest IRE_{MOA} occurred in spring (MAM), with the seasonal mean values of $-1.2 \sim -3.0$ W m^{-2} over vast areas from the East China Sea to the oceans east of Japan (Figure 10h). IRE_{MOA} in SON was similar in distribution pattern to that in MAM, with lower values in the above regions (Figure 10j). The IRE_{MOA} was weakest in JJA, with the maximum up to -1.5 W m^{-2} over a portion of the western Pacific east of Japan (Figure 10i), whereas the IRE_{MOA} value in DJF was between those in MAM and JJA with a similar distribution pattern. IRE_{MOA} is statistically significant at the 99% level over specific areas of EYB and NWP in all seasons. The seasonal variation of IRE_{MOA} was likely influenced by both the seasonal changes in cloud amount and MOA concentration. In terms of domain average, the seasonal mean IRE_{MOA} was strongest (-0.94 W m^{-2}) in MAM over the western Pacific (Table 10), which was mainly attributed to the maximum MOA concentration in spring (Table 8). IRE_{MOA} was secondly strongest in SON (-0.7 W m^{-2}) because MOA concentration and cloud fraction (Figure S3j) were both high in autumn. The weakest IRE_{MOA} occurred in JJA, which was mainly attributed to both the lower MOA concentration and cloud fraction in summer (Table 8, Figure S3i). Figure S4 further presents the monthly mean distributions of Chl-a concentration, MPOA emission, MOA concentration, and IRE_{MOA} in April, when Chl-a concentration and MPOA emission resulting from phytoplankton were distinctly high in the EYB and NWP regions (Figure S4a and S4b). It can be found that MOA was transported from the high Chl-a regions to the southeast under northwesterly winds over the oceans (Figure S4c), resulting in an elevated IRE_{MOA} up to -5 W m^{-2} over the western Pacific east of Japan (Figure S4d). Previous studies were very limited to compare with. Meskhidze and Nenes (2006) estimated based on satellite retrievals a reduction of 15 W m^{-2} in shortwave radiation at TOA due to changes in cloud properties during a strong phytoplankton bloom event near South Georgia Island in the Southern Ocean in summertime.

In terms of annual and regional mean, IRE_{MOA} was estimated to be -0.66 W m^{-2} for the western Pacific, -0.23 W m^{-2} over the EYB region, and -1.0 W m^{-2} over the NWP region, respectively (Table 10). There was an apparent seasonality in the IRE_{MOA}, with the maximum of -0.94 W m^{-2} in MAM and the minimum of -0.36 W m^{-2} in JJA over the western Pacific (Table 10). However, the seasonality

of IRE_{MOA} in the EYB and NWP regions are different from that over the western Pacific. Over the EYB, the estimated IRE_{MOA} reached its maximum (-0.38 W m^{-2}) in SON, which was due to the combined effect of a moderately high MOA concentration (Table 8) and the maximum cloud fraction (Figure S3j) in this region. Although MOA concentration reached the maximum in MAM, there was a minimum total cloud fraction in spring among seasons (Figure S3h), leading to a moderate IRE_{MOA}. Over the NWP region, IRE_{MOA} in DJF (-0.57 W m^{-2}) was smaller than those in other seasons (-0.78 ~ -1.4 W m^{-2}), which was mainly attributed to the lowest MOA concentration in winter (Table 8), although cloud fraction was highest among seasons in this region (Figure S3g).

The relative importance of MOA in the aerosol indirect radiative effect over the western Pacific was investigated by comparing the IRE_{MOA} with the IREs induced by sea salt and anthropogenic aerosols. In terms of annual and oceanic average, the IREs by sea salt and anthropogenic aerosols were estimated to be -0.41 W m^{-2} and -7.7 W m^{-2} (Table 10), respectively, indicating IRE_{MOA} (-0.66 W m^{-2}) was larger than the IRE by sea salt and was approximately 9% of that by anthropogenic aerosols. Although the hygroscopicity of sea salt is larger than that of MOA, because the mean radius of MOA (0.05 μm) is smaller than the radius of sea salt (0.1 μm for fine mode), the number concentration of MOA is larger than that of sea salt, leading to larger activated cloud droplet number concentration and IRE by MOA than those by sea salt. It is noted that the relative magnitude of IRE_{MOA} compared with the IRE by anthropogenic aerosols was reduced (5%) in the EYB and enhanced over the NWP (12%), because anthropogenic aerosols from the East Asian continent dominated aerosol magnitude in the marginal seas of China. In terms of seasonal and domain average over the western Pacific, IRE_{MOA} was approximately 1.6 times the IRE by sea salt, and approximately 10% of the IRE by anthropogenic aerosols in MAM. In summer (JJA) when both sea salt and anthropogenic aerosol concentrations were lowest, IRE_{MOA} was similar in magnitude to the IRE by sea salt, and about 8% of the IRE by anthropogenic aerosols. In the EYB region, IRE_{MOA} was just about 5% of the IRE by anthropogenic aerosols, but approximately three times the IRE by sea salt. In the NWP, IRE_{MOA} was about 12% of the IRE by anthropogenic aerosols in terms of annual mean, whereas in autumn when anthropogenic aerosol level was relatively low, IRE_{MOA} was as high as the maximum in MAM and approximately 18% of the IRE by anthropogenic aerosols. The above model estimation demonstrates that IRE_{MOA} was generally stronger than the IRE due to sea salt over the western Pacific, and approximately 6~18% of the IRE due to anthropogenic aerosols in the four seasons over the NWP, suggesting an important role

of MOA in perturbing radiation transfer through modifying cloud properties over the western Pacific Ocean of East Asia. The estimated IRE due to MSOA accounted for approximately 1% of the annual mean IRE_{MOA} averaged over the western Pacific, consistent with the very low proportion of MSOA in the MOA mass concentration (Table 8). Overall, MSOA plays a minor role in perturbing cloud properties and shortwave radiation compared with MPOA.

To address potential uncertainty in the estimated IRE_{MOA} due to limited knowledge on MOA properties, three additional sensitivity simulations from the base case (results shown in Figure S5 and Table S4) were carried out regarding particle size, solubility, and molecule weight, which are crucial to aerosol activation (note we focus on MPOA due to its dominant fraction in MOA as shown above). The first sensitivity simulation (SENS1) assumes a smaller geometric mean radius (0.02μm instead of 0.05μm in the base case) for MPOA, resulting in a weaker domain-annual mean IRE_{MOA} (-0.53 W m^{-2}) than that in the base case (-0.66 W m^{-2}) over the oceanic region (Figure S5b, Table S4). The second sensitivity simulation (SENS2) assigns a lower solubility (0.05) with relatively large molecule weight (146 g mol^{-1}) for MPOA (which is similar to the properties of adipic acid, Huff Hartz et al., 2006; Miyazaki et al., 2010) instead of the slight solubility (0.1) with a smaller molecule weight (90 g mol^{-1}) (which is similar to the properties of oxalic acid, Roelofs, 2008; Miyazaki et al., 2010) in the base case, in this case, the IRE_{MOA} reduces to -0.2 W m^{-2} (Figure S5c, Table S4). The third simulation (SENS3) combines the above two cases, assuming a smaller geometric mean radius as in SENS1 together with the lower solubility and larger molecule weight as in SENS2, it produces a further reduced IRE_{MOA} of -0.14 W m^{-2} (Figure S5d, Table S4). The above sensitivity simulations exhibit a high sensitivity of IRE_{MOA} to the MPOA properties.

It is interesting to note that Quinn et al. (2017) indicated that sea spray aerosol generally makes a contribution of less than 30% to CCN population at supersaturation of 0.1 to 1.0% on a global basis based on measurements onboard seven research cruises over the Pacific, Southern, Arctic and Atlantic oceans. However, their cruise tracks did not cover the western Pacific Ocean. The results from this study exhibits the annual and oceanic mean contribution of sea spray aerosol (the sum of MOA and sea salt) to the IRE by total aerosols was approximately 12% in the base case over the western Pacific region (Table 10). This percentage contribution increases to 19% in the NWP in autumn due to the highest IRE_{MOA} and lower IRE by anthropogenic aerosols in autumn (Table 10).

The western Pacific Ocean is just downwind of the East Asian continent, which have large

1081 amounts of anthropogenic aerosols, mineral dust, and nutrients inputs to the marginal seas of China

1082 from the Yangtze and Yellow Rivers, could be very different from remote clean oceans in the world.

1083 Although some cruise measurements have been carried out and a few knowledges on MOA properties

1084 (e.g., size distribution) was gained, the cruise measurement and observational analysis for MOA

1085 chemical properties are so far almost absent in the western Pacific of East Asia. Therefore, marine

1086 biogeochemistry, marine aerosol sources and properties, as well as their potentials to be CCN and

1087 impacts on radiation, cloud, and precipitation deserve further investigation in the future.

1088

1089 4.5 Indirect radiative effect of MOA due to aerosol-radiation and aerosol-cloud interactions

1090 IPCC AR5 proposes the concept of effective radiative forcing (ERF), which is defined as the

1091 change in net radiative flux at TOA after rapid adjustment of the atmosphere (including atmospheric

1092 temperature, water vapor, cloud, circulation) to radiation perturbation with prescribed SST and sea ice,

1093 which can better represent climate response to perturbation of forcing factors (Boucher et al., 2013).

1094 Similarly, this study also estimates the direct radiative effect of MOA due to aerosol-radiation

1095 interaction (denoted as DRE_{ari} hereinafter) and the indirect radiative effect of MOA due to

1096 aerosol-cloud interaction (denoted as IRE_{aci} hereinafter). Note the method for calculating DRE_{ari} and

1097 IRE_{aci} is different from that for DRE_{MOA} and IRE_{MOA}. DRE_{ari} is derived by the difference in shortwave

1098 radiation flux at TOA induced by MOA scattering between two simulations with aerosol optical

1099 properties due to total aerosols and with those due to total aerosols but MOA, while the perturbation

1100 of MOA to cloud properties is turned off. IRE_{aci} is calculated by the difference in shortwave radiation

1101 flux at TOA induced by MOA perturbation to cloud albedo between two simulations with cloud

1102 properties due to total aerosols and with those due to total aerosols but MOA, while the direct

1103 perturbation of MOA to radiation is closed. The calculation of DRE_{ari} and IRE_{aci} considers the

1104 adjustment of atmospheric temperature, water vapor, and cloud (including cloud microphysical and

1105 lifetime change, i.e., the second indirect effect) to the MOA-induced radiation perturbation in the two

1106 simulations.

1107 Figure 11a shows the annual mean MOA DRE_{ari} in the study domain. The distribution of MOA

1108 DRE_{ari} was similar in distribution to that of DRE_{MOA} without statistical significance at the 99% level.

1109 It is noted that DRE_{ari} was not consistently negative in the domain, the effect of atmospheric

1110 adjustment on radiation can be seen in some locations over the Ocean and the continent, with a few

1111   positive values of $0.1\sim0.3$ W m^{-2}.

1112   Figure 11b shows the annual mean MOA IRE_{aci} in the study domain, which was similar in

1113   magnitude and distribution pattern to IRE_{MOA} (Figure 10f), but it distributed unevenly in the domain

1114   with some positive values exceeding 0.2 W m^{-2} over both the Western Pacific and the continent. IRE_{aci}

1115   of MOA was statistically significant at the 99% confidence level over the NWP region. The

1116   atmospheric response and adjustment induced by IRE_{MOA} could be somewhat stronger than that by

1117 DRE_{MOA}, with respect to the positive values of IRE_{aci} up to 0.3 W m^{-2} over the continent. The small

1118   positive values could be associated with the radiative feedback and atmospheric and cloud adjustment.

1119   The annual and domain average of DRE_{ari} and IRE_{aci} over the western Pacific are estimated to be

1120   -0.25 W m^{-2} and -0.61 W m^{-2}, respectively, both are somewhat weaker than the DRE_{MOA} (-0.27 W m^{-2})

1121   and IRE_{MOA} (-0.66 W m^{-2}).

1122

1123   5. Conclusions.

1124   The organic aerosols of marine origin over the western Pacific Ocean of East Asia was

1125   investigated by an online-coupled regional climate-chemistry model RIEMS-Chem for the year 2014.

1126   Emissions and relevant processes of marine MPOA, isoprene and monoterpene were incorporated into

1127   RIEMS-Chem. A wide variety of observational datasets from EANET, CNEMC and AERONET

1128   networks, cruise measurements and previous publications were collected for model validation. The

1129   modeled SOA from marine VOC sources was also compared with secondary organic tracers measured

1130   by research cruise. The model performed well for PM$_{2.5}$ and PM$_{10}$ in marine environment, producing

1131   overall correlation coefficients and NMBs of 0.61/0.70 and 12%/-7% for PM$_{2.5}$ concentration,

1132   0.65/0.65 and -5%/-1% for PM$_{10}$ concentration at the EANET/CNEMC sites, respectively. The model

1133   reasonably reproduced the spatial distribution and temporal variation of BC and OC concentrations

1134   along cruise tracks and at islands over the west Pacific, with the correlation coefficients and NMBs

1135   being $0.6\sim0.75$ and $-28\%\sim3\%$ for OC, respectively. The modeled OC concentration was apparently

1136   improved while taking into account marine organic aerosols. The model results clearly showed an

1137   increasing contribution of marine organic aerosols to total OC mass concentration from the marginal

1138   seas of China to remote oceans. Organic aerosol mass of marine origin was dominated by MPOA

1139   because MSOA produced by marine isoprene and monoterpene emissions was about $1\sim2$ orders of

1140   magnitude lower than MPOA. The model simulates AOD reasonably well at the 7 coastal or island

1141 AERONET sites, with an overall correlation coefficient of 0.54 and an NMB of -6%.

1142 High MPOA emission mainly occurred over the marginal seas of China (EYB) and the northern

1143 parts of western Pacific northeast of Japan (NWP). For the western Pacific, MPOA emission reached

1144 the maximum in SON, followed by those in DJF and MAM, and the minimum in JJA, with an annual

1145 and domain average emission rate of 0.16×10^{-2} μg m^{-2} s^{-1}. The combination of Chl-a concentration and

1146 sea salt emission flux determined the seasonality of MPOA emission. The annual MPOA emission for

1147 the year 2014 was estimated to be 0.78 Tg yr^{-1} over the western Pacific.

1148 Consistent with the distribution pattern MPOA emission, high MOA concentration mainly

1149 distributed over the EYB and NWP, with an annual and domain mean concentration of 0.27 μg m^{-3},

1150 0.48 μg m^{-3} and 0.59 μg m^{-3}, over the western Pacific, the EYB and NWP regions, respectively. MOA

1151 concentration was highest in MAM and lowest in DJF, with the seasonal and domain mean values of

1152 0.37 μg m^{-3} and 0.21 μg m^{-3}, respectively, over the western Pacific. The seasonality of MOA

1153 concentration was determined by the combined effect of MPOA emission, dry and wet depositions.

1154 On average, the annual mean percentage contribution of MOA to total OA mass was 26% over the

1155 western Pacific, with the largest seasonal mean contribution of 32% in SON and the lower ones in

1156 DJF (24%) and JJA (23%). Over the NWP, the domain average contribution of MOA to OA could be

1157 as high as 42% in terms of annual mean and approaching 52% in MAM; however, over the EYB, the

1158 annual mean contribution was just 13% and the percentage contribution was even reduced to 6% in

1159 JJA. This indicated that the relative importance of MOA in total OA concentration increased with the

1160 distance away from the East Asian continent. MSOA concentration was approximately 1~2 orders of

1161 magnitude lower than MPOA, with the simulated annual and regional mean MSOA being 2.2 ng m^{-3}

1162 and the maximum daily mean value up to 28 ng m^{-3} in summer over the western Pacific.

1163 An annual/oceanic mean all-sky DRE_{MOA} of -0.27 W m^{-2} at TOA was estimated over the western

1164 Pacific, which was about 40% of the IRE_{MOA} (-0.66 W m^{-2}). The domain mean IRE_{MOA} was strongest

1165 in spring (-0.94 W m^{-2}) and weakest in summer (-0.36 W m^{-2}) over the western Pacific, and the

1166 monthly mean IRE_{MOA} can reach -5 W m^{-2} in the NWP region east of Japan in April. The changes in

1167 MOA concentration and cloud amount both contributed to the seasonality of IRE_{MOA}. In terms of

1168 annual and oceanic mean over the western Pacific, MSOA just contributed approximately 1% of the

1169 IRE_{MOA}. IRE_{MOA} was generally larger than the IRE due to sea salt on average. The annual and oceanic

1170 mean IRE due to sea spray aerosols (MOA + sea salt) was approximately 12% of that due to total

aerosols over the western Pacific, but this ratio can increase up to 19% in autumn in the NWP region. The estimation of IRE_{MOA} was sensitive to MOA properties, which decreased apparently while a smaller geometric mean radius together with a lower solubility and a larger molecule weight were assigned for MOA. Overall, the indirect radiative effect of MOA was larger than the direct radiative effect, and had a nonnegligible impact on radiation budget and cloud over the western Pacific. The direct and indirect radiative effect considering atmospheric feedback and adjustment were estimated as well, which was similar in magnitude to the DRE_{MOA} and IRE_{MOA}, with a few positive changes in shortwave radiation fluxes in some locations.

While this study presents new insights into the seasonal variation and annual means of emissions, concentrations, and radiative effects of MOA in the western Pacific, it is still subject to some uncertainties as follows: 1.) the properties of marine organic aerosols, including size distribution, molecular weight, solubility, surfactant amount etc. are still poorly characterized, which are crucial to aerosol activation, dry deposition, and wet scavenging; 2.) the sources and chemical formation processes of marine organic aerosols including secondary organics are highly complex, and poorly understood and represented in the model; 3.) the indirect effects of MOA in this study is for warm stratiform cloud. Further research on MOA sources, properties, chemical processes, and climatic impacts will be conducted together with the advances in both field experiments (integrated cruise, aircraft and satellite observations) and model development in the future.

Author Contributions.

ZH designed the study, JL and ZH developed the model, processed and analyzed the model results, JL performed the model simulation, ZH and JL wrote the paper, PF and XY provided and analyzed the cruise measurement data, ML analyzed the model results.

Data availability.

The observational data can be accessed through contacting the corresponding author.

Competing interests.

The authors declare that they have no conflict of interests.

Acknowledgement.

This study was supported by the National Key R&D Program of China (No. 2019YFA0606802), the National Natural Science Foundation of China (No. 42275118, No. 42375107), the Jiangsu Collaborative Innovation Center for Climate Change. The authors appreciate the science teams of EANET, CNEMC, AERONET, MODIS and VIIRS for their works in data maintenance.

Reference

Abdul-Razzak, H., Ghan, S. J., and Rivera-Carpio, C.: A parameterization of aerosol activation: 1. Single aerosol type, J. Geophys. Res., 103, 6123–6131, 1998.

Abdul-Razzak, H. and Ghan, S. J.: Parameterization of the influence of organic surfactants on aerosol activation, J. Geophys. Res., 109, D03205, doi:10.1029/2003JD004043, 2004.

Arnold, S.R., Spracklen, D.V., Williams, J., Yassaa, N., Sciare, J., Bonsang, B., Gros, V., Peeken, I., Lewis, A.C., Alvain, S., andMoulin, C.: Evaluation of the global oceanic isoprene source and its impacts on marine organic carbon aerosol, Atmos. Chem. Phys., 9, 1253–1262. https://doi.org/10.5194/acp-9-1253-2009, 2009.

Bates, T. S., Quinn, P. K., Coffman, D. J., Johnson, J. E., Upchurch, L., Saliba, G., Lewis, S., Graff, J., Russell, L. M., and Behrenfeld, M. J.: Variability in Marine Plankton Ecosystems Are Not Observed in Freshly Emitted Sea Spray Aerosol Over the North Atlantic Ocean, Geophy. Res. Lett., 47, e2019GL085938. https://doi.org/10.1029/2019GL085938, 2020.

Beheng, K.D.: A parameterization of warm cloud microphysical conversion processes. Atmos. Res., 33, 193–206. https://doi.org/10.1016/0169-8095(94)90020-5, 1994.

Bertram, T. H., Cochran, R. E., Grassian, V. H., and Stone, E. A.: Sea spray aerosol chemical composition: elemental and molecular mimics for laboratory studies of heterogeneous and multiphase reactions, Chem. Soc. Rev., 47(7), 2374-2400, DOI: 10.1039/c7cs00008a, 2018.

Bennartz, R.: Global assessment of marine boundary layer cloud droplet number concentration from satellite, J. Geophys. Res.,112, D02201, doi:10.1029/2006jd007547, 2007.

Bikkina, S., Kawamura, K., Miyazaki, Y., and Fu, P.: High abundances of oxalic, azelaic and glyoxylic acids and methylglyoxal in the open ocean with high biological activity: Implication for secondary OA formation from isoprene, Geophys. Res. Lett., 41, 3649–3657, 2014.

Booge, D., Marandino, C.A., Schlundt, C., Palmer, P.I., Schlundt, M., Atlas, E.L., Bracher, A.,

Saltzman, E.S., and Wallace, D.W.R.: Can simple models predict large-scale surface ocean isoprene concentrations? Atmos. Chem. Phys., 16, 11807–11821, https://doi.org/10.5194/acp-16-11807-2016, 2016.

Boreddy, S.K.R., Haque, M.M., and Kawamura, K.: Long-term (2001–2012) trends of carbonaceous aerosols from a remote island in the western North Pacific: an outflow region of Asian pollutants, Atmos. Chem. Phys., 18, 1291–1306, https://doi.org/10.5194/acp-18-1291-2018, 2018.

Boucher, O., Randall, D., Artaxo, P., Bretherton, C., Feingold, G., Forster, P., et al.: Clouds and aerosols. In T. F. Stocker, et al. (Eds.), Climate change 2013: The physical science basis. Contribution of working group I to the fifth assessment report of the Intergovernmental Panel on Climate Change (pp. 616–632). Cambridge: Cambridge University Press, 2013.

Brüggemann, M., Hayeck, N. and George, C.: Interfacial photochemistry at the ocean surface is a global source of organic vapors and aerosols, Nat. Commun., 9, 2101. https://doi.org/10.1038/s41467-018-04528-7, 2018.

Burrows, S. M., Ogunro, O., Frossard, A. A., Russell, L. M., Rasch, P. J., and Elliott, S. M.: A physically based framework for modeling the organic fractionation of sea spray aerosol from bubble film Langmuir equilibria, Atmos. Chem. Phys., 14, 13601–13629, https://doi.org/10.5194/acp-14-13601-2014, 2014.

Burrows, S. M., Easter, R. C., Liu, X., Ma, P.-L., Wang, H., Elliott, S. M., Singh, B., Zhang, K., and Rasch, P. J.: OCEANFILMS (Organic Compounds from Ecosystems to Aerosols: Natural Films and Interfaces via Langmuir Molecular Surfactants) sea spray organic aerosol emissions – implementation in a global climate model and impacts on clouds, Atmos. Chem. Phys., 22, 5223–5251, https://doi.org/10.5194/acp-22-5223-2022, 2022.

Calil, P.H.R., Doney, S.C., Yumimoto, K., Eguchi, K., Takemura, T.: Episodic upwelling and dust deposition as bloom triggers in low-nutrient, low-chlorophyll regions, J. Geophys. Res.: Oceans, 116, C06030. http://dx.doi.org/10.1029/2010JC006704, 2011.

Chang, J.S., Brost, R.A., Isaksen, I.S.A., Madronich, S., Middleton, P., Stockwell, W.R., Walcek, C.J.: A three-dimensional Eulerian acid deposition model: physical concepts and formulation, J. Geophys. Res., 92(D12), 14681-14700, doi:10.1029/JD092iD12p14681, 1987.

Conte, L., Szopa, S., Aumont, O., Gros, V., and Bopp, L.: Sources and sinks of isoprene in the global open ocean: Simulated patterns and emissions to the atmosphere, J. Geophys. Res: Oceans, 125,

e2019JC015946. https://doi.org/10.1029/2019JC015946, 2020.

Curci, G., Hogrefe, C., Bianconi, R., Im, U., Balzarini, A., Baró, R., Brunner, D., Forkel, R., Giordano, L., Hirtl, M., Honzak, L., Jiménez-Guerrero, P., Knote, C., Langer, M., Makar, P. A., Pirovano, G., Pérez, J. L., San José, R., Syrakov, D., Tuccella, P., Werhahn, J., Wolke, R., Žabkar, R., Zhang, J., and Galmarini, S.: Uncertainties of simulated aerosol optical properties induced by assumptions on aerosol physical and chemical properties: An AQMEII-2 perspective, Atmos. Environ., 115, 541–552, 2015.

Dickinson, R.E., Henderson-Sellers, A., Kennedy, P.J.: Biosphere-Atmosphere Transfer Scheme (BATS) Version 1e as coupled to NCAR Community Climate Model, NCAR Technical Note, NCAR/TN-387+STR, p. 72, 1993.

Emmons, L.K., Walters, S., Hess, P.G., Lamarque, J.-F., Pfister, G.G., Fillmore, D., Granier, C., Guenther, A., Kinnison, D., Laepple, T., Orlando, J., Tie, X., Tyndall, G., Wiedinmyer, C., Baughcum, S.L., and Kloster, S.: Description and evaluation of the Model for Ozone and Related chemical Tracers, version 4 (MOZART-4), Geosci. Model Dev., 3, 43-67, doi:10.5194/gmd-3-43-2010, 2010.

Facchini, M.C., Rinaldi, M., Decesari, S., Carbone, C., Finessi, E., Mircea, M., Fuzzi, S., Ceburnis, D., Flanagan, R., Nilsson, E.D., de Leeuw, G., Martino, M., Woeltjen, J., and O'Dowd, C.D.: Primary submicron marine aerosol dominated by insoluble organic colloids and aggregates, Geophys. Res. Lett., 35, L17814, doi:10.1029/2008GL034210, 2008.

Feng, L.M., Shen, H.Q., Zhu, Y.J., Gao, H.W., and Yao, X.H.: Insight into Generation and Evolution of Sea-Salt Aerosols from Field Measurements in Diversified Marine and Coastal Atmospheres, Sci. Rep., 7, 41260; doi: 10.1038/srep41260, 2017.

Fountoukis, C. and Nenes, A.: ISORROPIA II: a computationally efficient thermodynamic equilibrium model for K^+–Ca^{2+}–Mg^{2+}–NH_4^+–Na^+–SO_4^{2-}–NO_3^-–Cl^-–H_2O aerosols, Atmos. Chem. Phys., 7, 4639-4659, 2007.

Fröhlich-Nowoisky Janine, Christopher J. Kampf, Bettina Weber, J. Alex Huffman, Christopher Pöhlker, Meinrat O. Andreae, Naama Lang-Yona, Susannah M. Burrows, Sachin S. Gunthe, Wolfgang Elbert, Hang Su, Peter Hoor, Eckhard Thines, Thorsten Hoffmann, Viviane R. Després, Ulrich Pöschl: Bioaerosols in the Earth system: Climate, health, and ecosystem interactions. Atmospheric Research, 182, 346-376, 2016.

Fu, C. B., Wang, S.Y., Xiong, Z., Gutowski, W. J., Lee, D., Mcgregor, J. L., Sato, Y., Kato, H., Kim, J., Suh, M.: Regional climate model intercomparison project for Asia, Bull. Amer. Meteor. Soc., 86, 257-266, 2005.

Fu, P., Kawamura, K., and Miura, K.: Molecular characterization of marine organic aerosols collected during a round‐the‐world cruise, J. Geophys. Res., 116, D13302, doi:10.1029/2011JD015604, 2011.

Gantt, B., Meskhidze, N., and Kamykowski, D.: A new physically-based quantification of marine isoprene and primary organic aerosol emissions, Atmos. Chem. Phys., 9, 4915-4927, https://doi.org/10.5194/acp-9-4915-2009, 2009.

Gantt, B., Meskhidze, N., Facchini, M.C., Rinaldi, M., Ceburnis, D., and O'Dowd, C.D.: Wind speed dependent size-resolved parameterization for the organic mass fraction of sea spray aerosol, Atmos. Chem. Phys., 11, 8777-8790, https://doi.org/10.5194/acp-11-8777-2011, 2011.

Gantt, B., Johnson, M. S., Meskhidze, N., Sciare, J., Ovadnevaite, J., Ceburnis, D., and O'Dowd, C. D.: Model evaluation of marine primary organic aerosol emission schemes, Atmos. Chem. Phys., 12, 8553-8566, https://doi.org/10.5194/acp-12-8553-2012, 2012a.

Gantt, B., Xu, J., Meskhidze, N., Zhang, Y., Nenes, A., Ghan, S. J., Liu, X., Easter, R., and Zaveri, R.: Global distribution and climate forcing of marine organic aerosol – Part 2: Effects on cloud properties and radiative forcing, Atmos. Chem. Phys., 12, 6555-6563, https://doi.org/10.5194/acp-12-6555-2012, 2012b.

Gantt, B. and Meskhidze, N.: The physical and chemical characteristics of marine primary organic aerosol: a review, Atmos. Chem. Phys., 13, 3979–3996, 2013.

Gao, M., Han, Z., Liu, Z., Li, M., Xin, J., Tao, Z., Li, J., Kang, J.-E., Huang, K., Dong, X., Zhuang, B., Li, S., Ge, B., Wu, Q., Cheng, Y., Wang, Y., Lee, H.-J., Kim, C.-H., Fu, J. S., Wang, T., Chin, M., Woo, J.-H., Zhang, Q., Wang, Z., and Carmichael, G. R.: Air quality and climate change, Topic 3 of the Model Inter-Comparison Study for Asia Phase III (MICS-Asia III) – Part 1: Overview and model evaluation, Atmos. Chem. Phys., 18, 4859-4884, 2018.

Gery, M. W., Whitten, G. Z., Killus, J. P., Dodge, M. C.. A photochemical kinetics mechanism for urban and regional scale computer modeling, J. Geophys. Res., 94, 12925-12956, 1989.

Ghan, S. J., Leung, L. R., Easter, R. C., Abdul-Razzak, K.: Prediction of cloud droplet number in a general circulation model, J. Geophys. Res., 102 (D18), 21,777–21,794, 1997.

Ghan, S. and Zaveri R.A.: Parameterization of optical properties for hydrated internally mixed aerosol, J. Geophys. Res., 112, D10201, doi:10.1029/2006JD007927, 2007.

Giglio, L., Randerson, J.T., and van der Werf, G.R.: Analysis of daily, monthly, and annual burned area using the fourth generation Global Fire Emissions Database (GFED4), J. Geophys. Res.: Biogeosciences, doi:10.1002/jgrg.20042, 2013.

Gong, S. L., L. A. Barrie, and J.-P. Blanchet: Modeling sea-salt aerosols in the atmosphere 1. Model development, J. Geophys. Res., 102(D3), 3805-3818, doi:10.1029/96JD02953, 1997.

Gong, S. L., X. Zhang, T. Zhao, I. G. Mckendry, D. A. Jaffe, and N. Lu: Characterization of soil dust aerosol in China and its transport and distribution during 2001 ACE-Asia: 2. Model simulation and validation, J. Geophys. Res., 108(D9), 4262, doi:10.1029/2002JD002633, 2003.

Gong, S.L.: A parameterization of sea-salt aerosol source function for sub- and super-micron particles, Global Biogeochem. Cy., 17(4), 1097, doi:10.1029/2003GB002079, 2003.

Graf, H.-F., Feichter, J., and Langmann, B.: Volcanic sulfur emissions: Estimates of source strength and its contribution to the global sulfate distribution. J. Geophys. Res., 102(D9), 10727-10738, doi: 10.1029/96JD03265, 1997.

Granier, C., Darras, S., Denier van der Gon, H., Doubalova, J., Elguindi, N., Galle, B., Gauss, M., Guevara, M., Jalkanen, J.-P., Kuenen, J., Liousse, C., Quack, B., Simpson, D., and Sindelarova, K.: The Copernicus Atmosphere Monitoring Service global and regional emissions (April 2019 version), Report April 2019 version, doi:10.24380/d0bn-kx16, 2019.

Grell, G.A.: Prognostic evaluation of assumptions used by cumulus parameterizations, Mon. Wea. Rev. 121, 764-787, 1993.

Grell, G.A., Dudhia, J., Stauffer, D.R.: A Description of the Fifth-Generation Penn State/NCAR Mesoscale Model (MM5), NCAR Technical Note, NCAR/TN-398tSTR, p.117, 1995.

Guo, T., Guo, Z., Wang, J., Feng, J., Gao, H., and Yao, X.: Tracer-based investigation of organic aerosols in marine atmospheres from marginal seas of China to the northwest Pacific Ocean, Atmos. Chem. Phys., 20, 5055–5070, https://doi.org/10.5194/acp-20-5055-2020, 2020.

Han, X., Zhang, M. G., Han, Z. W., Xin, J. Y., Liu, X. H.: Simulation of aerosol direct radiative forcing with RAMS-CMAQ in East Asia, Atmos. Environ., 45, 6576-6592, 2011.

Han, Z.: Direct radiative effect of aerosols over East Asia with a regional coupled climate/chemistry model, Meteor. Zeit., 19, 287–298, 2010.

Han, Z. W., Ueda, H., Matsuda, K., Zhang, R. J., Arao, K., Kanai, Y., Hasome, H.: Model study on particle size segregation and deposition during Asian dust events in March 2002, J. Geophys. Res., 109, D19205, doi:10.1029/2004jd004920, 2004.

Han, Z.W., Li, J.W., Xia, X.A., Zhang, R.J.: Investigation of direct radiative effects of aerosols in dust storm season over East Asia with an online coupled regional climate-chemistry-aerosol model, Atmos. Environ., 54, 688-699, 2012.

Han, Z.W., Li, J.W., Guo, W.D., Xiong, Z., Zhang, W.: A study of dust radiative feedback on dust cycle and meteorology over East Asia by a coupled regional climate-chemistry-aerosol model, Atmos. Environ., 68, 54-63, 2013.

Han, Z.W., Li, J.W., Yao, X.H., Tan, S.C.: A regional model study of the characteristics and indirect effects of marine primary organic aerosol in springtime over East Asia, Atmos. Environ., 197, 22–35, 2019.

Hsiao, T.-C., Chen, W.-N., Ye, W.-C., Lin, N.-H., Tsay, S.-C., Lin, T.-H., Lee, C.-T., Chuang, M.-T., Pantina, P., Wang, S.-H.: Aerosol optical properties at the Lulin Atmospheric Background Station in Taiwan and the influences of long-range transport of air pollutants, Atmos. Environ., 150, 366-378, 2017.

Hong, S. H. and Pan, H. L.: Nonlocal boundary layer vertical diffusion in a medium range forecast model, Mon. Wea. Rev., 124, 2322–2339, 1996.

Hoose, C., Kristjánsson, J. E., Iversen T., A. Kirkevag, Ø. Seland, and Gettelman A.: Constraining cloud droplet number concentration in GCMs suppresses the aerosol indirect effect, Geophys. Res. Lett., 36, L12807, doi:10.1029/2009GL038568, 2009.

Hu, Q.-H., Xie, Z.-Q., Wang, X.-M., Kang, H., He, Q.-F., and Zhang, P.: Secondary organic aerosols over oceans via oxidation of isoprene and monoterpenes from Arctic to Antarctic, Sci. Rep., 3, 2280, doi:10.1038/srep02280, 2013.

Huang, W. T. K., Ickes, L., Tegen, I., Rinaldi, M., Ceburnis, D., and Lohmann, U.: Global relevance of marine organic aerosol as ice nucleating particles, Atmos. Chem. Phys., 18, 11423–11445, https://doi.org/10.5194/acp-18-11423-2018, 2018.

Huff Hartz, K. E., Tischuk, J. E., Chan, M, N., Chan, C. K., Donahue, N. M., and Pandis, S. N.: Cloud condensation nuclei activation of limited solubility organic aerosol, Atmospheric Environment 40, 605–617, 2006.

1381 IPCC: Intergovernmental Panel on Climate Change, Climate Change 2013: The Physical Science

1382   Basis. Contribution of Working Group I to the Fifth Assessment Report of the Intergovernmental

1383   Panel on Climate Change, Report, edited by: Stocker, T.F., Qin, D.H., Plattner, G.K., Tignor,

1384   M.M.B., Allen, S. K., Boschung, J., Nauels, A., Xia, Y., Bex, V., and Midgley, P.M., Cambridge

1385   University Press, New York, http://www.ipcc.ch/report/ar5, 2013 (last access: 2020/04/30).

1386 Kanaya, Y., Pan, X., Miyakawa, T., Komazaki, Y., Taketani, F., Uno, I., and Kondo, Y.: Long-term

1387   observations of black carbon mass concentrations at Fukue Island, western Japan, during 2009–

1388   2015: constraining wet removal rates and emission strengths from East Asia, Atmos. Chem. Phys.,

1389   16, 10689–10705, https://doi.org/10.5194/acp-16-10689-2016, 2016.

1390 Kang, M., Fu, P., Kawamura, K., Yang, F., Zhang, H., Zang, Z., Ren, H., Ren, L., Zhao, Y., Sun, Y.,

1391   and Wang, Z.: Characterization of biogenic primary and secondary organic aerosols in the marine

1392   atmosphere over the East China Sea, Atmos. Chem. Phys., 18, 13947–13967, 2018.

1393 Kelly, J. T., Bhave, P. V., Nolte, C. G., Shankar, U., and Foley, K. M.: Simulating emission and

1394   chemical evolution of coarse sea-salt particles in the Community Multiscale Air Quality (CMAQ)

1395   model. Geosci. Model Dev., 3, 257–273, 2010.

1396 Kiehl, J.T., Hack, J.J., Bonan, G.B., Boville, B.A., Briegleb, B.P., Williamson, D.L., Rasch, P.J.:

1397   Description of the NCAR Community Climate Model (CCM3), NCAR Technical Note,

1398   NCAR/TN-420+STR, p.152, 1996.

1399 Kunwar, B. and Kawamura, K.: One-year observations of carbonaceous and nitrogenous components

1400   and major ions in the aerosols from subtropical Okinawa Island, an outflow region of Asian dusts,

1401   Atmos. Chem. Phys., 14, 1819–1836, https://doi.org/10.5194/acp-14-1819-2014, 2014.

1402 Lack, D. A., Tie, X. X., Bofinger, N. D., Wiegand, A. N., and Madronich, S.: Seasonal variability of

1403   secondary organic aerosol: A global modeling study, J. Geophys. Res.: Atmosphere, 109, D03203,

1404   doi:10.1029/2003JD003418, 2004.

1405 Lee, A., Goldstein, A. H, Kroll, J. H., Ng, N. L., Varutbangkul, V., Flagan, R. C., and Seinfeld, J. H.:

1406   Gas-phase products and secondary aerosol yields from the photooxidation of 16 different

1407   terpenes, J. Geophys. Res., 111, D17305, doi:10.1029/2006JD007050, 2006.

1408 Leibensperger, E. M., Mickley, L. J., Jacob, D. J., Chen, W.-T., Seinfeld, J. H., Nenes, A., Adams, P. J.,

1409   Streets, D. G., Kumar, N., and Rind, D.: Climatic effects of 1950–2050 changes in US

1410   anthropogenic aerosols–Part 1: Aerosol trends and radiative forcing, Atmos. Chem. Phys., 12,

3333–3348, 2012.

Li, J.-L., Zhang, H.-H., and Yang, G.-P.: Distribution and sea-to-air flux of isoprene in the East China Sea and the South Yellow Sea during summer, Chemosphere, 178, 291-300, 2017.

Li, J.-L., Zhai, X., Zhang, H.-H., and Yang, G.-P.: Temporal variations in the distribution and sea-to-air flux of marine isoprene in the East China Sea, Atmos. Environ., 187, 131–143, 2018.

Li, J.W. and Han, Z.W.: A modeling study of the impact of heterogeneous reactions on mineral aerosol surfaces on tropospheric chemistry over East Asia, Particuology, 8, 433-441, 2010.

Li, J.W., Han, Z.W., and Zhang, R.J.: Influence of aerosol hygroscopic growth parameterization on aerosol optical depth and direct radiative forcing over East Asia, Atmos. Res., 140-141, 14-27, 2014.

Li, J. W. and Han, Z. W.: Aerosol vertical distribution over east china from RIEMS-Chem simulation in comparison with CALIPSO measurements, Atmos. Environ., 143, 177-189, 2016a.

Li, J. W. and Han, Z. W.: Seasonal variation of nitrate concentration and its direct radiative forcing over East Asia, Atmosphere, 7(8), 105, 2016b.

Li, J. W., Han, Z. W., Yao, X. H.: A modeling study of the influence of sea salt on inorganic aerosol concentration, size distribution, and deposition in the western Pacific Ocean, Atmos. Environ., 188, 157-173, 2018.

Li, J. W., Han, Z. W., Yao, X. H., Xie, Z. X., Tan, S. C.: The distributions and direct radiative effects of marine aerosols over East Asia in springtime, Sci. Tot. Environ., 651, 1913–1925, 2019.

Li, J., Han, Z., Wu, Y., Xiong, Z., Xia, X., Li, J., Liang, L., and Zhang, R.: Aerosol radiative effects and feedbacks on boundary layer meteorology and PM2.5 chemical components during winter haze events over the Beijing-Tianjin-Hebei region, Atmos. Chem. Phys., 20, 8659–8690, https://doi.org/10.5194/acp-20-8659-2020, 2020.

Li, M., Zhang, Q., Kurokawa, J.-I., Woo, J.-H., He, K., Lu, Z., Ohara, T., Song, Y., Streets, D.G., Carmichael, G.R., Cheng, Y., Hong, C., Huo, H., Jiang, X., Kang, S., Liu, F., Su, H., and Zheng, B.: MIX: a mosaic Asian anthropogenic emission inventory under the international collaboration framework of the MICS-Asia and HTAP, Atmos. Chem. Phys., 17, 935-963, doi:10.5194/acp-17-935-2017, 2017.

Liao, H., Seinfeld, J.H., Adams, P.J., Mickley, L.J.: Global radiative forcing of coupled tropospheric ozone and aerosols in a unified general circulation model, J. Geophys. Res.: Atmosphere, 109,

D16207. https://doi.org/10.1029/2003JD004456, 2004.

Liu, X. and Wang, J.: How important is organic aerosol hygroscopicity to aerosol indirect forcing? Environ. Res. Lett., 5(4), 044010, http://iopscience.iop.org/1748-9326/5/4/044010, 2010.

Lohmann, U. and Feichter J.: Global indirect aerosol effects: a review, Atmos. Chem. Phys., 5, 715–737, 2005.

Long, M. S., Keene, W. C., Kieber, D. J., Erickson, D. J., and Maring, H.: A sea-state based source function for size- and composition-resolved marine aerosol production, Atmos. Chem. Phys., 11, 1203–1216, https://doi.org/10.5194/acp-11-1203-2011, 2011.

Luo, G. and Yu, F.: A numerical evaluation of global oceanic emissions of a-pinene and isoprene, Atmos. Chem. Phys., 10, 2007–2015, doi:10.5194/acp-10-2007-2010, 2010.

Luo, L., Yao, X.H., Gao, H.W., Hsu, S.C., Li, J.W., and Kao, S.J.: Nitrogen speciation in various types of aerosols in spring over the northwestern Pacific Ocean, Atmos. Chem. Phys., 16, 325-341, 2016.

Luo, L., Kao, S.-J., Bao, H., Xiao, H., Xiao, H., Yao, X., Gao, H., Li, J., and Lu, Y.: Sources of reactive nitrogen in marine aerosol over the Northwest Pacific Ocean in spring, Atmos. Chem. Phys., 18, 6207–6222, 2018.

Ma, Q. X., Wu, Y. F., Zhang, D. Z., Wang, X. J., Xia, Y. J., Liu, X. Y., Tian, P., Han, Z. W., Xia, X. A., Wang, Y., and Zhang, R. J.: Roles of regional transport and heterogeneous reactions in the PM2.5 increase during winter haze episodes in Beijing, Sci. Total. Environ., 599/600, 246–253, 2017.

Martin, G. M., Johnson, D. W., and Spice, A.: The Measurements and Parameterization of Effective Radius of Droplets in Warm Stratocumulus Clouds, J. Atmos. Sci., 51, 1823–1842, 1994.

Matsunaga, S., Mochida, M., Saito, T., and Kawamura, K.: In situ measurement of isoprene in the marine air and surface seawater from the western North Pacific, Atmos. Environ., 36, 6051–6057, doi:10.1016/s1352-2310(02)00657-x, 2002.

Meskhidze, N. and Nenes, A.: Phytoplankton and cloudiness in the Southern Ocean, Science, 314, 1419–1423, 2006.

Meskhidze, N., Xu, J., Gantt, B., Zhang, Y., Nenes, A., Ghan, S.J., Liu, X., Easter, R., Zaveri, R.: Global distribution and climate forcing of marine organic aerosol: 1. Model improvements and evaluation, Atmos. Chem. Phys., 11, 11689–11705, 2011.

Miyazaki Yuzo, Kawamura Kimitaka, and Sawano Maki: Size distributions and chemical

characterization of water-soluble organic aerosols over the western North Pacific in summer, J. Geophys. Res., 115, D23210, doi:10.1029/2010JD014439, 2010.

Monahan, E. C., Spiel, D. E., Davidson, K. L.: A model of marine aerosol generation via white caps and wave disruption. In: Oceanic Whitecaps. D. Reidel, Norwell, Mass, pp. 167–174, 1986.

Myriokefalitakis, S., Vignati, E., Tsigaridis, K., Papadimas, C., Sciare, J., Mihalopoulos, N., Facchini, M.C., Rinaldi, M., Dentener, F.J., Ceburnis, D., Hatzianastasiou, N., O'Dowd, C.D., van Weele, M., and Kanakidou, M.: Global modeling of the oceanic source of organic aerosols. Adv. Meteor., 939171, doi:10.1155/2010/939171, 2010.

NOAA/NCEP: NCEP FNL Operational Model Global Tropospheric Analyses, continuing from July 1999. Research Data Archive at the National Center for Atmospheric Research, Computational and Information Systems Laboratory. Dataset. https://doi.org/10.5065/D6M043C6, 2000, Last accessed, 2019/12/12.

OBPG: NASA Goddard Space Flight Center, Ocean Ecology Laboratory, Ocean Biology Processing Group: Visible and Infrared Imager/Radiometer Suite (VIIRS) Chlorophyll Data; NASA OB.DAAC, Greenbelt, MD, USA. doi:10.5067/NPP/VIIRS/L3M/CHL/2018.

O'Dowd, C.D., Facchini, M.C., Cavalli, F., Ceburnis, D., Mircea, M., Decesari, S., Fuzzi, S., Yoon, Y.J., Putaud, J.P.: Biogenically driven organic contribution to marine aerosol, Nature, 431, 676–680, 2004.

Ooki, A., Nomura, D., Nishino, S., Kikuchi, T., and Yokouchi, Y.: A global-scale map of isoprene and volatile organic iodine in surface seawater of the Arctic, Northwest Pacific, Indian, and Southern Oceans, J. Geophys. Res.: Oceans 120, 4108–4128, doi:10.1002/2014JC010519, 2015.

Ovadnevaite, J., Ceburnis, D., Martucci, G., Bialek, J., Monahan, C., Rinaldi, M., Facchini, M.C., Berresheim, H., Worsnop, D.R., O'Dowd, C.: Primary marine organic aerosol: a dichotomy of low hygroscopicity and high CCN activity, Geophys. Res. Lett., 38, L21806. https://doi.org/10.1029/2011GL048869, 2011.

Petters, M.D. and Kreidenweis, S.M.: A single parameter representation of hygroscopic growth and cloud condensation nucleus activity, Atmos. Chem. Phys., 7, 1961-1971, 2007.

Quinn, P. K., Bates Timothy S., Schulz Kristen S., Coffman D. J., Frossard A. A., Russell L. M., Keene W. C. and Kieber D. J.. Contribution of sea surface carbon pool to organic matter enrichment in sea spray aerosol. Nat. Geosci. 7, 228-232, 2014.

Quinn, P. K., Coffman, D. J., Johnson, J. E., Upchurch, L. M., and Bates, T. S.: Small fraction of marine cloud condensation nuclei made up of sea spray aerosol, Nat. Geosci., 10, 674–679, 2017.

Rap, A., Scott, C.E., Spracklen, D.V., Bellouin, N., Forster, P.M., Carslaw, K.S., Schmidt, A., and Mann, G.: Natural aerosol direct and indirect radiative effects, Geophys. Res. Lett., 40, 3297-3301, doi:10.1002/grl.50441, 2013.

Reisner, J., Rasmussen, R.M., Bruintjes, R.T.: Explicit forecasting of super cooled liquid water in winter storms using the MM5 mesoscale model, Quart. J. Roy. Meteor. Soc., 124 (548), 1071–1107, 1998.

Riemer, N., West, M., Zaveri, R., Easter, R.: Estimating black carbon aging time-scales with a particle-resolved aerosol model, J. Aerosol Sci., 41, 143-158, 2010.

Roelofs, G.J.: A GCM study of organic matter in marine aerosol and its potential contribution to cloud drop activation, Atmos. Chem. Phys., 8, 709–719 2008, 2008.

Sayer, A. M., Hsu, N. C., Bettenhausen, C., Lee, J., Kim, W. V., and Smirnov, A.: Satellite Ocean Aerosol Retrieval (SOAR) Algorithm Extension to S-NPP VIIRS as Part of the "Deep Blue" Aerosol Project, J. Geophys. Res. Atmos., 123, doi:10.1002/2017JD027412, 2018.

Shao, Y. and Dong, C.H.: A review on East Asian dust storm climate, modeling and monitoring, Glob. Planet. Change, 52, 1-22, 2006.

Sindelarova, K., Granier, C., Bouarar, I., Guenther, A., Tilmes, S., Stavrakou, T., Müller, J.-F., Kuhn, U., Stefani, P., and Knorr, W.: Global data set of biogenic VOC emissions calculated by the MEGAN model over the last 30 years. Atmos. Chem. Phys., 14, 9317–9341. https://doi.org/10.5194/acp-14-9317-2014, 2014.

Slingo A.: A GCM Parameterization for the Shortwave Radiative Properties of Water Clouds, J. Atmos. Sci., 46(10), 1419-1427, 1989.

Slinn, W. G. N.: Precipitation scavenging: in Atmospheric Science and Power Production. pp. 466–532, Technical Information Center, Office of Science and Technology Information, Department of Energy, Washington, D. C., 1984.

Smith, S.J., van Aardenne, J., Klimont, Z., Andres, R.J., Volke, A., and Delgado Arias, S.: Anthropogenic sulfur dioxide emissions: 1850-2005, Atmos. Chem. Phys., 11, 1101-1116, 2011.

Spracklen, D.V., Arnold, S.R., Carslaw, K.S., Sciare, J., and Pio, C.: Globally significant oceanic source of organic carbon aerosol, Geophys. Res. Lett., 35, L12811, doi:10.1029/2008GL033359,

1531   2008.

1532 Surratt, J. D., Chan, A. W. H., Eddingsaas, N. C., Chan, M. N., Loza, C. L., Kwan, A. J., Hersey, S. P.,

1533   Flagan, R. C., Wennberg, P. O., and Seinfeld, J. H.: Reactive intermediates revealed in secondary

1534   organic aerosol formation from isoprene, P. Natl. Acad. Sci. USA, 107, 6640–6645,

1535   doi:10.1073/pnas.0911114107, 2010.

1536 Tan, S. C., Li, J. W., Che, H. Z., Chen, B., and Wang, H.: Transport of East Asian dust storms to the

1537   marginal seas of China and the southern North Pacific in spring 2010, Atmos. Environ., 148,

1538   316-328, 2017.

1539 Tao, J., Surapipith, V., Han, Z. W., Prapamontol, T., Kawichai, S., Zhang, L. M., Zhang, Z. S., Wu, Y.

1540   F., Li, J. W., Li J., Yang, Y. H., and Zhang, R. J.: High mass absorption efficiency of

1541   carbonaceous aerosols during the biomass burning season in Chiang Mai of northern Thailand,

1542   Atmos. Environ., 240, 117821, 2020.

1543 Van den Berg, A., Dentener, F., and Lelieveld, J.,: Modeling the chemistry of the marine boundary

1544   layer: Sulphate formation and the role of sea-salt aerosol particles, J. Geophys. Res., 105, 11671–

1545   11698. https://doi.org/10.1029/1999JD901073, 2000.

1546 Vignati, E., Facchini, M.C., Rinaldi, M., Scannell, C., Ceburnis, D., Sciare, J., Kanakidou, M.,

1547   Myriokefalitakis, S., Dentener, F., and O'Dowd, C.D.. Global scale emission and distribution of

1548   seaspray aerosol: sea-salt and organic enrichment, Atmos. Environ., 44, 670–677, 2010.

1549 Xiong, Z., Fu, C. B., and Yan, X. D.: Regional Integrated environmental model system and its

1550   simulation of East Asia summer monsoon, Chinese Sci. Bull., 54(22), 4253-4261, 2009.

1551 Wang, F. W., Guo, Z. G., Lin, T., Hu, L. M., Chen, Y. J., and Zhu, Y. F.: Characterization of

1552   carbonaceous aerosols over the East China Sea: The impact of the East Asian continental outflow,

1553   Atmos. Environ., 110, 163-173, 2015.

1554 Wang, M., and Penner J. E.: Aerosol indirect forcing in a global model with particle nucleation, Atmos.

1555   Chem. Phys., 9, 239– 260, 2009.

1556 Wang, S. Y., Fu, C. B., Wei, H. L., Qian, Y., Xiong, Z., Feng, J. M., Zhao, D. M., Dan, L., Han, Z. W.,

1557   Su, B. K., Zhao, M., Zhang, Y. C., Tang, J. P., Liu, H. N., Wu, J., Zeng, X. M., Chen, M., Wang,

1558   L. Z.: Regional integrated environmental modeling system: development and application,

1559   Climatic Change, 129, 499-510, 2015.

1560 Westervelt, D. M., Moore, R. H., Nenes, A., and Adams, P. J.: Effect of primary organic sea spray

emissions on cloud condensation nuclei concentrations, Atmos. Chem. Phys., 12, 89–101. https://doi.org/10.5194/acp-12-89-2012, 2012.

Wu, Y. F., Wang, X. J., Tao, J., Huang, R. J., Tian, P., Cao, J. J., Zhang, L. M., Ho, K. F., Han, Z. W., Zhang, R. J.: Size distribution and source of black carbon aerosol in urban Beijing during winter haze episodes, Atmos. Chem. Phys., 17, 7965-7975, 2017.

Zeng, S., Riedi, J., Trepte, C. R., Winker, D. M. & Hu, Y. X.: Study of global cloud droplet number concentration with A-Train satellites. Atmos. Chem. Phys. 14, 7125–7134, 2014.

Zhang, K. M., Knipping, E. M., Wexler, A. S., Bhave, P. V., and Tonnesen, G. S.: Size distribution of sea-salt emissions as a function of relative humidity, Atmos. Environ., 39, 3373-3379, 2005.

Zhang, L. M., Gong, S. L., Padro, J., and Barrie, L.: A size-segregated particle dry deposition scheme for an atmospheric aerosol module, Atmos. Environ., 35(3), 549-560, 2001.

Zhao, B., Liou, K. N., Gu, Y., Li, Q., Jiang, J. H., Su, H., He, C., Tseng, H. R., Wang, S., Liu, R., Qi, L., Lee, W. L., and Hao, J.: Enhanced $PM_{2.5}$ pollution in China due to aerosol-cloud interactions, Sci. Rep., 7, 4453, https://doi.org/10.1038/s41598-017-04096-8, 2017.

Zhu, C., Kawamura, K., and Fu, P.: Seasonal variations of biogenic secondary organic aerosol tracers in Cape Hedo, Okinawa, Atmos. Environ., 130, 113-119, 2016.
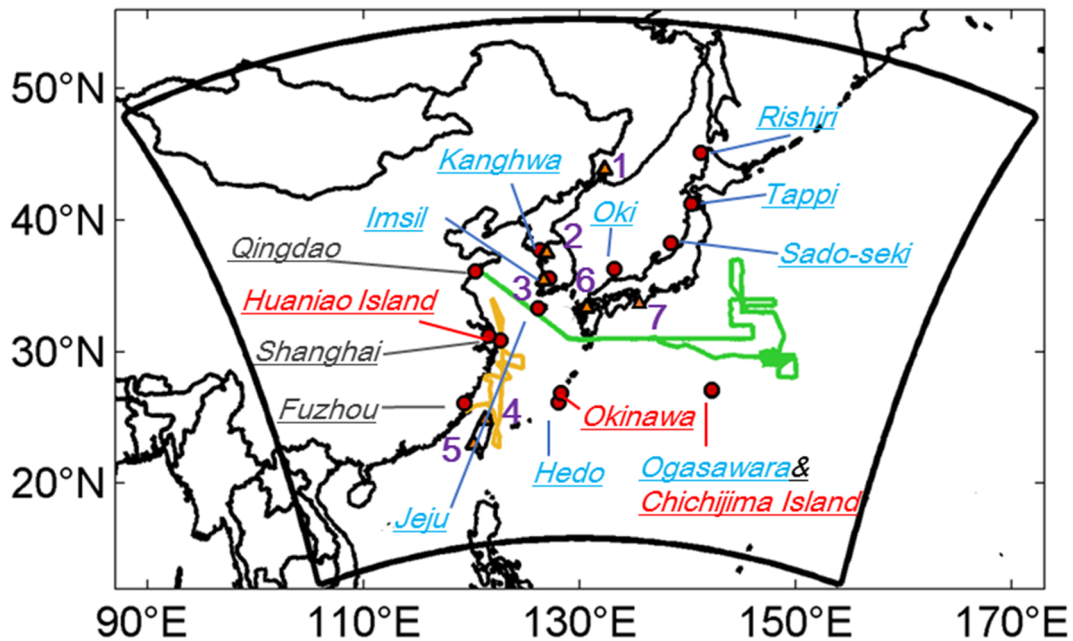
Figure 1. Model domain, observational sites, and research cruise tracks. EANET sites are marked in light-blue. Observation sites of carbonaceous aerosols are marked in red (Chichijima Island: Boreddy et al., 2018; Fukue: Kanaya et al., 2016; Okinawa: Kunwar and Kawamura, 2014; Huaniao Island: Wang F. W. et al., 2014). Three CNEMC sites are marked in grey (Qingdao, Shanghai, and Fuzhou). Two research cruise tracks are represented by green line (Dongfanghong II from 17 March to 22 April 2014: Luo et al., 2016; Feng et al., 2017) and orange line (KEXUE-1 from 18 May to 12 June 2014: Kang et al., 2018), respectively. AERONET sites are represented by triangles with numbers (1-Ussuriysk, 2-Yonsei_University, 3-Gwangju_GIST, 4-EPA-NCU, 5-Chen-Kung_Univ, 6-Fukuoka, and 7-Shirahama). Full names of abbreviations are given in the text.

Figure 2. The model simulated (Sim) and observed (Obs) monthly PM$_{10}$ (a~l) and PM$_{2.5}$ (m~r) concentrations at EANET and CNEMC sites for the year 2014. The monthly data were averaged from hourly observations and the simulations were sampled according to the observations. Simulated aerosol components (PPM: primary anthropogenic PM, Sea salt, Dust, MOA, Car: anthropogenic BC+OC, SNA: sulfate+nitrate+ammonium) are also shown.
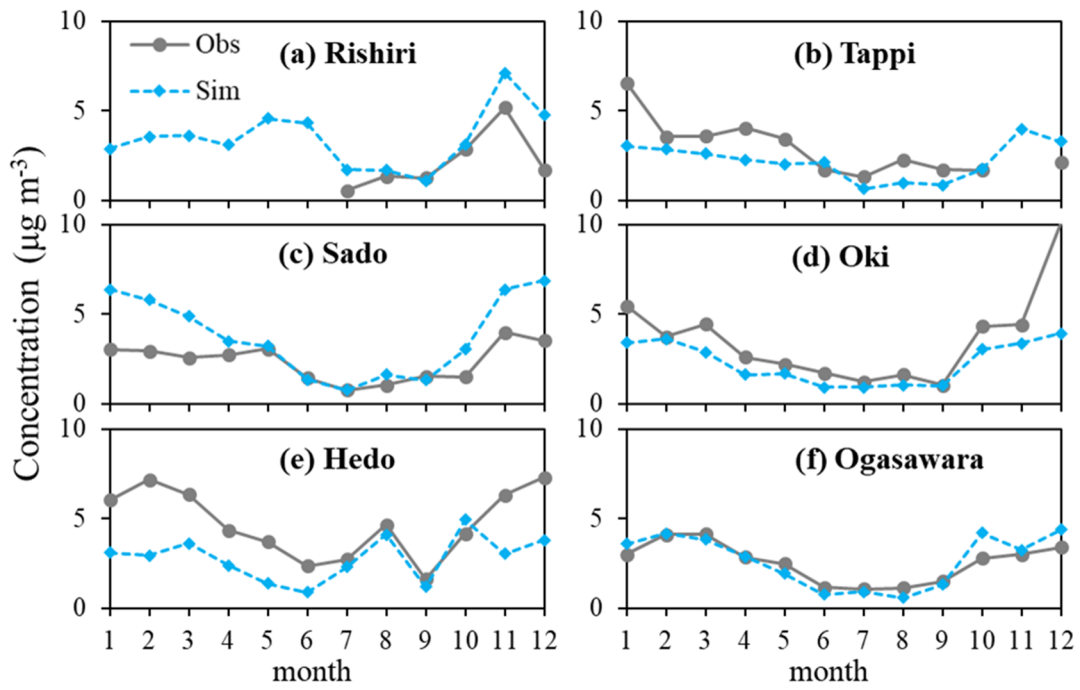
Figure 3. Observed and model simulated monthly mean sodium (Na+) concentrations at 6 coastal and island EANET sites of Japan for the year 2014.
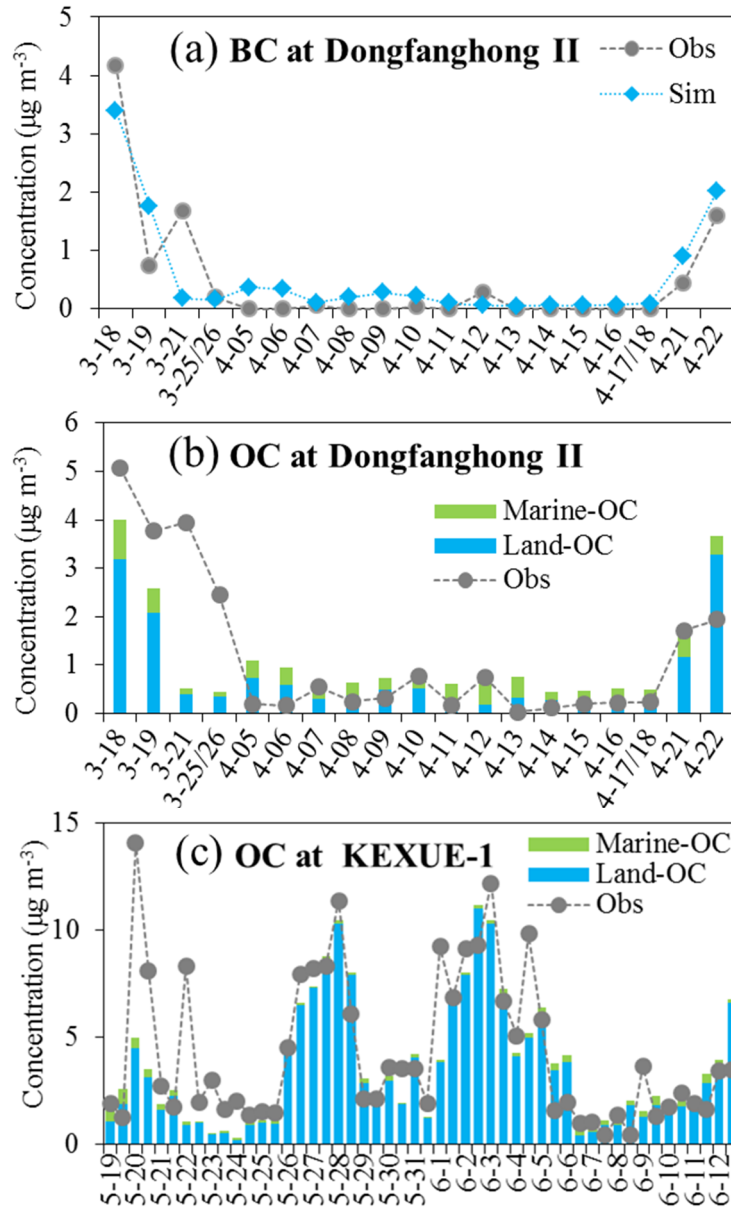
Figure 4. The model simulated (bars) and observed (dotted lines) daily BC and OC concentrations from the spring campaign (a, b) and half-day OC concentrations from the early summer campaign (c). The modeled total OC concentration was decomposed into those from marine (green bars) and land (blue bars) sources.
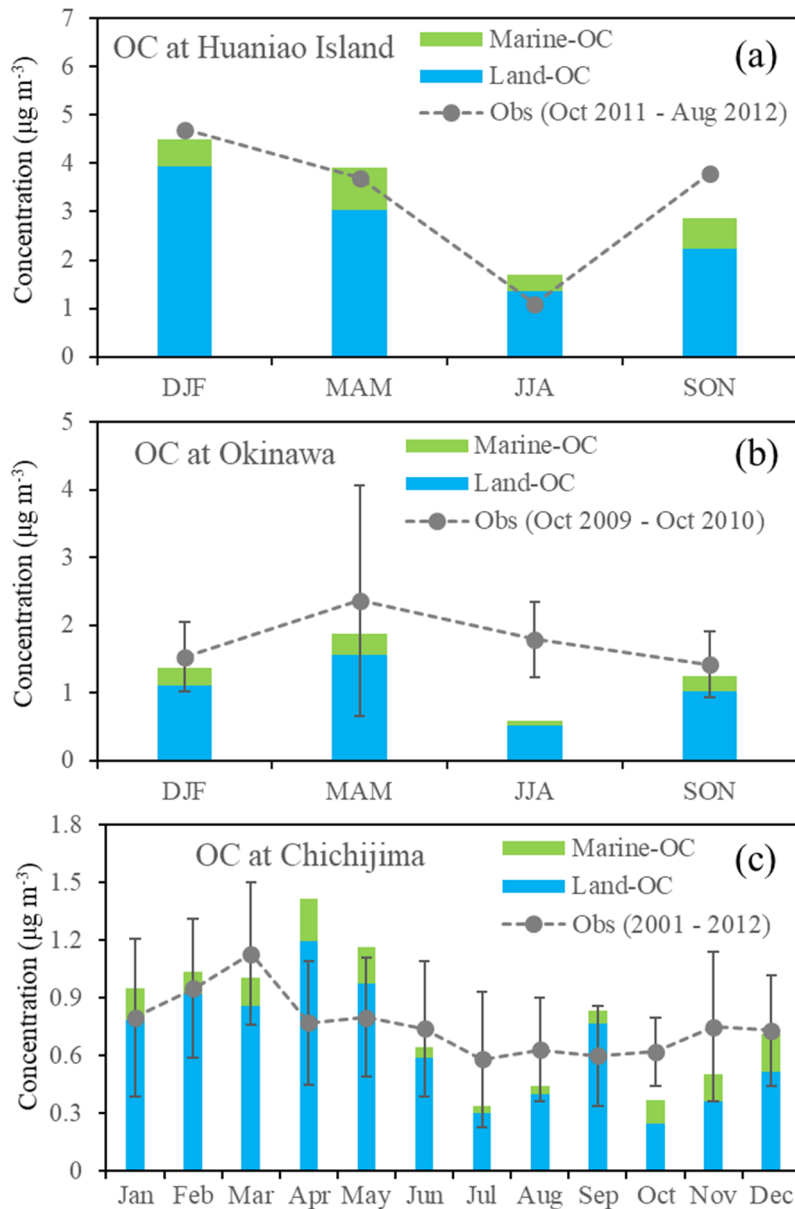
Figure 5. The model simulated (bars) and observed (dotted lines) OC concentrations at different sites. Seasonal mean concentrations were provided at (a) Huaniao Island (Wang et al., 2015) and (b) Okinawa (Kunwar and Kawamura, 2014) while monthly mean concentrations were provided at (c) Chichijima Island (Boreddy et al., 2018). Standard deviations were available at Okinawa and Chichijima. The modeled OC concentrations were decomposed to marine (green bars) and land (blue bars) sources. The simulation is for the year 2014.
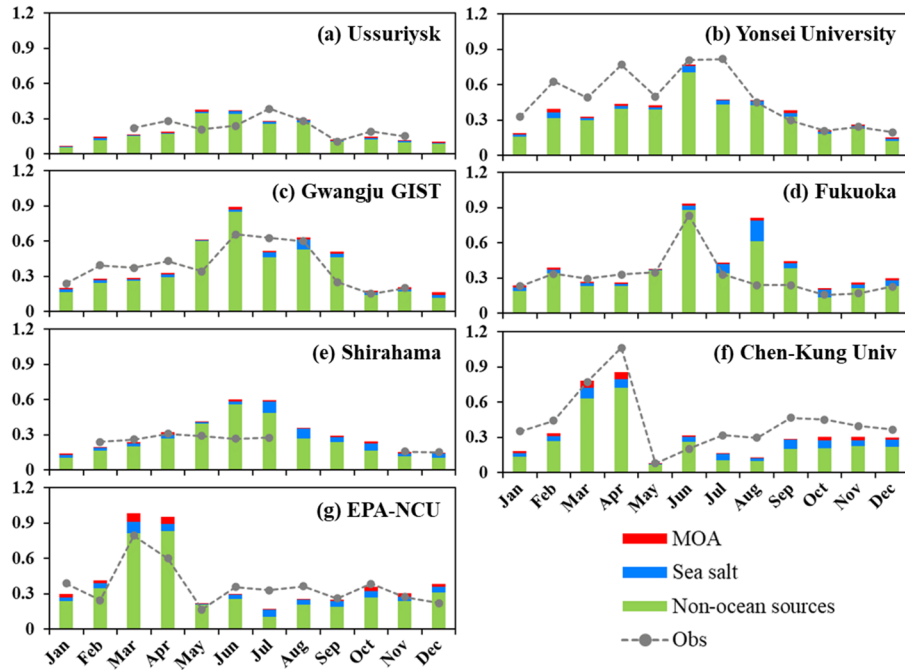
Figure 6. The model simulated (Sim) and observed (Obs) monthly mean AOD at 7 AERONET sites for the year 2014. The monthly mean observations were calculated from hourly data and the simulations were sampled according to the observations. Contributions of aerosol components to total AOD by MOA, sea salt, and aerosols of non-oceanic sources (anthropogenic, dust etc.) are shown.
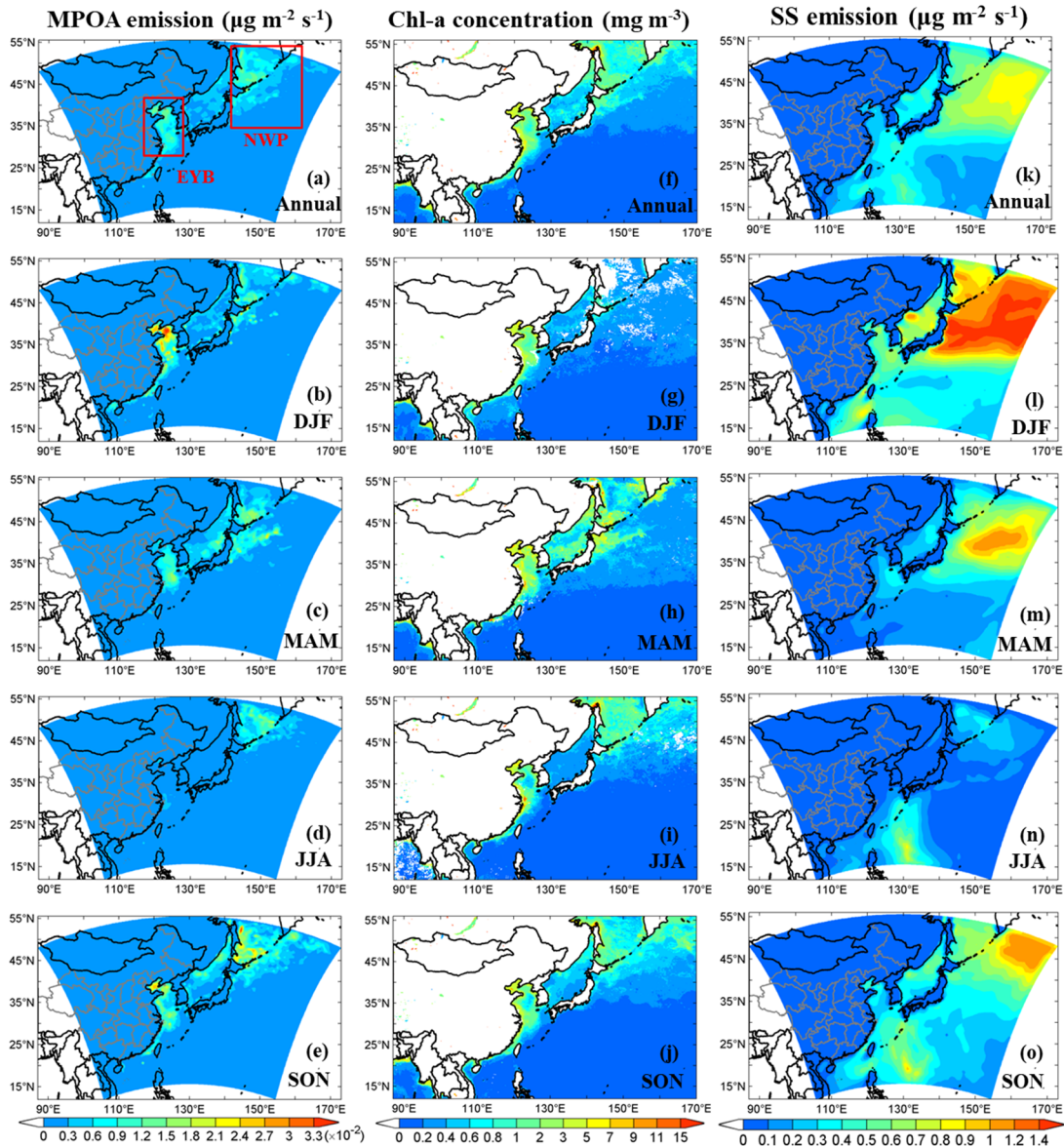
Figure 7. Model simulated annual and seasonal mean distributions of MPOA emissions (a~e), VIIRS retrieved surface sea water chlorophyll-a (Chl-a) concentrations (f~j), and model simulated sea salt (SS) emissions (k~o). Two hotspot regions are marked with red boxes: the region including the East China Sea, the Yellow Sea, and the Bohai Sea (EYB, 27~40°N, 115~123°E) and the region including the northern parts of the western Pacific to the northeast of Japan (NWP, 35~55°N, 140~160°E). Units are given in parentheses.
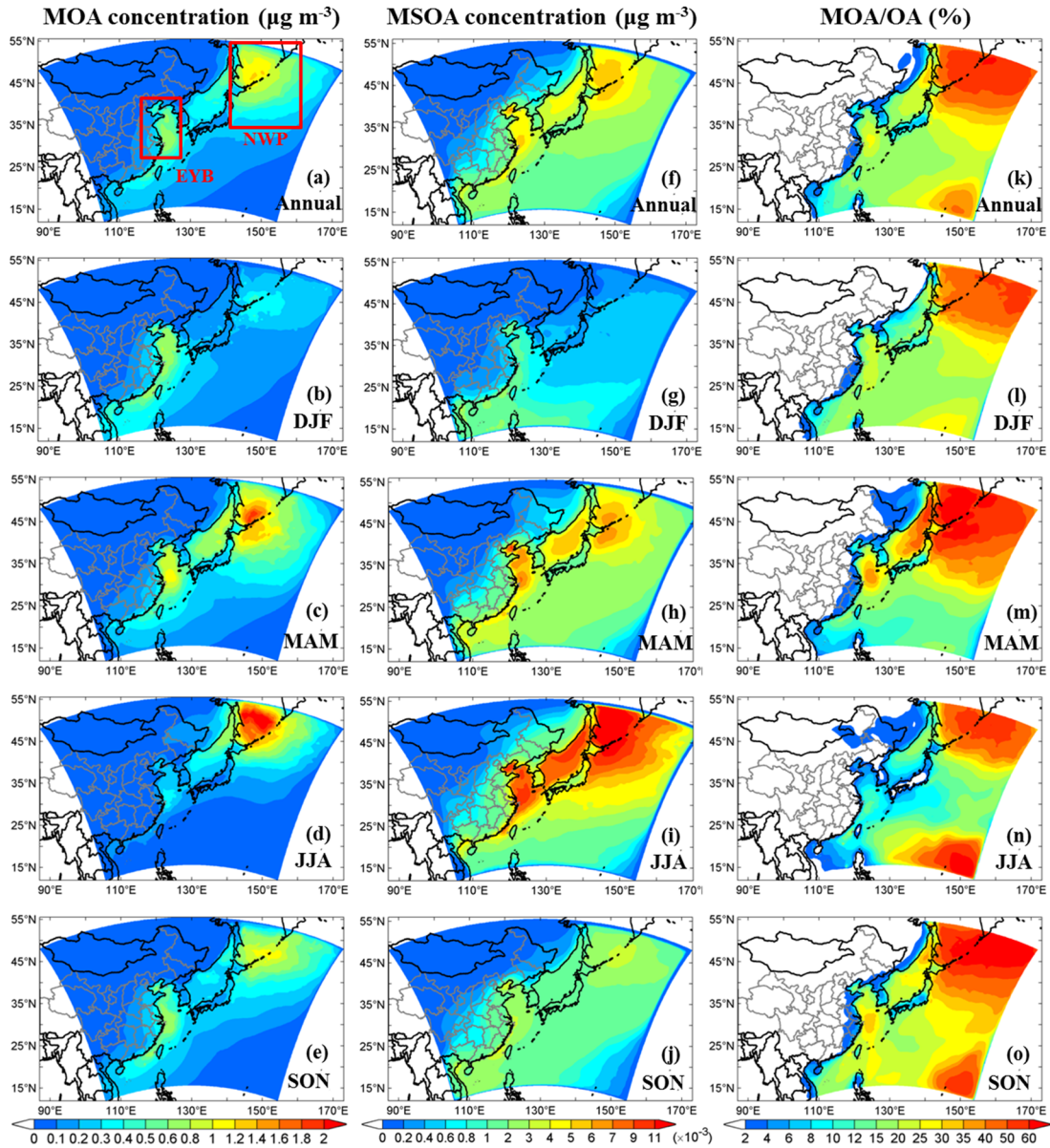
Figure 8. Model simulated annual and seasonal mean near surface MOA (primary+secondary) concentrations (a~e), near surface MSOA concentrations (f~j), and percentage contributions of MOA to total OA (k~o). The two regions of the EYB (27~40°N, 115~123°E) and the NWP (35~55°N, 140~160°E) are marked in 8a. Units are given in parentheses.
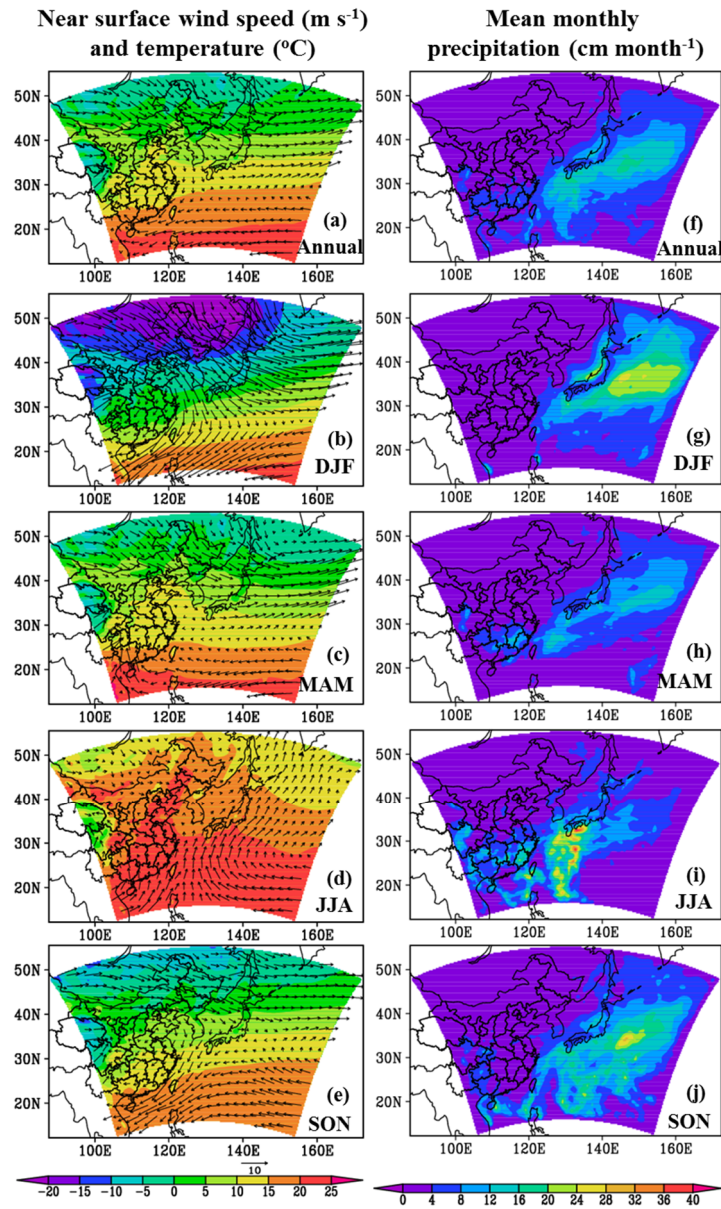
Figure 9. Model simulated annual and seasonal mean near surface temperatures (unite: °C) overlaid with wind vectors (unit: m s⁻¹) (a~e) and mean monthly precipitations (unit: cm month⁻¹) (f~j).
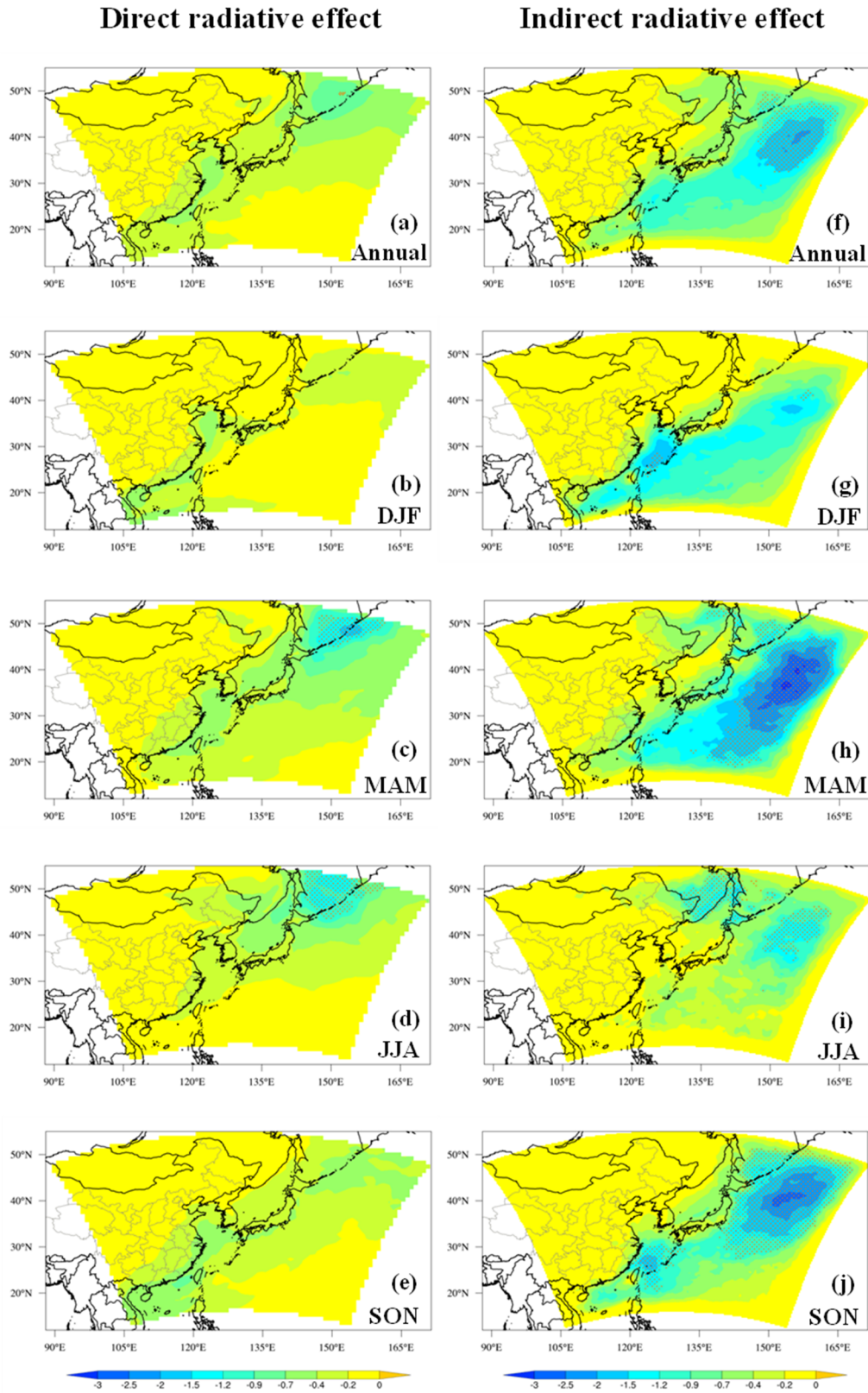
Figure 10. Model simulated annual and seasonal mean direct radiative effect due to MOA (DRE$_{MOA}$) (a~e) and indirect radiative effect due to MOA (IRE$_{MOA}$) (f~j) at the top of atmosphere (TOA) under all-sky condition (unit: W m^{-2}). Red dot indicates areas where the difference is statistically significant at the 99% confidence level according to a two-tailed t-test.
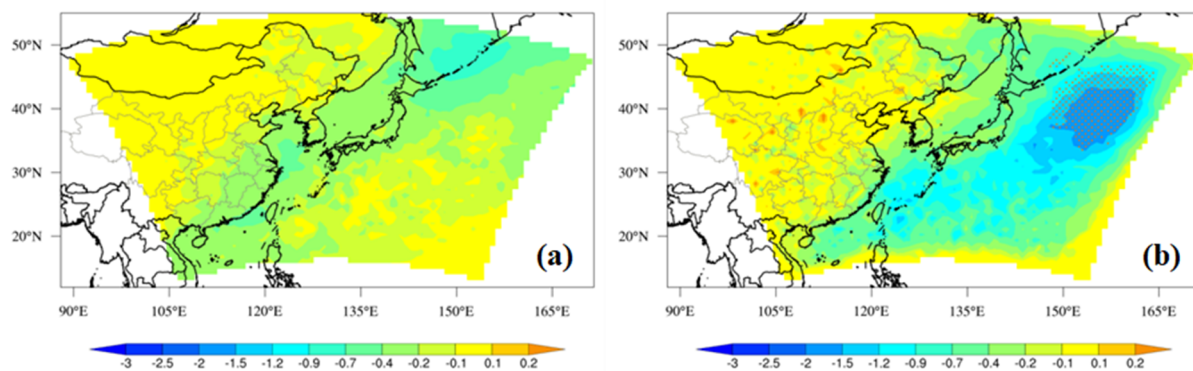
Figure 11. Model simulated annual mean (a) direct radiative effect of MOA due to aerosol-radiation interaction (DRE$_{ari}$), (b) indirect radiative effect of MOA due to aerosol-cloud interaction (IRE$_{aci}$) at the top of atmosphere (TOA) (unit: W m^{-2}). Red dot indicates areas where the difference is statistically significant at the 99% confidence level according to a two-tailed t-test.

Table 1. Annual and seasonal performance statistics for hourly PM_{10} and $PM_{2.5}$ concentrations (unit: $\mu g\ m^{-3}$) at EANET sites for the year 2014. Mean observation (Obs), mean simulation (Sim), correlation coefficient (R), and normalized mean bias (NMB in %) are listed. ANN=annual, DJF=December-January-February, MAM=March-April-May, JJA=June-July-August, and SON=September-October-November.

Sites	Samples	ANN				DJF				MAM				JJA				SON			
		Obs	Sim	R	NMB	Obs	Sim	R	NMB	Obs	Sim	R	NMB	Obs	Sim	R	NMB	Obs	Sim	R	NMB
PM_{10}																					
Rishiri	8381	18.0	19.9	0.53	11	13.6	18.4	0.65	35	20.1	23.0	0.56	15	15.2	19.4	0.42	28	23.0	18.8	0.51	-18
Tappi	8584	20.1	23.2	0.49	15	17.4	22.3	0.54	28	29.0	28.0	0.59	-4	16.1	23.8	0.18	48	17.6	18.5	0.39	5
Sado	8640	22.8	26.4	0.63	16	23.6	29.5	0.68	25	29.2	30.3	0.65	4	18.6	24.5	0.55	32	19.6	21.4	0.53	9
Oki	8424	31.3	29.2	0.68	-7	33.2	31.1	0.65	-7	40.2	37.5	0.71	-7	26.7	26.6	0.61	0	25.8	22.3	0.66	-14
Hedo	8008	27.7	21.7	0.56	-22	28.8	22.4	0.66	-22	30.5	28.3	0.58	-7	20.7	14.8	0.54	-28	30.9	20.8	0.34	-33
Ogasawara	8120	11.5	15.7	0.48	36	13.4	20.3	0.38	52	14.2	19.7	0.40	39	7.0	6.8	0.46	-2	11.2	15.0	0.30	34
Jeju	7101	46.9	36.9	0.64	-21	50.1	38.2	0.71	-24	62.6	46.6	0.66	-26	36.4	31.5	0.44	-13	34.7	29.3	0.44	-15
Kanghwa	8524	49.2	51.2	0.59	4	50.2	46.0	0.60	-8	59.9	61.9	0.66	3	40.0	47.2	0.47	18	46.5	49.3	0.38	6
Imsil	8383	44.5	32.3	0.58	-27	48.8	27.9	0.63	-43	58.0	42.1	0.62	-27	38.4	31.1	0.47	-19	33.0	28.2	0.42	-15
Average	74165	30.0	28.5	0.65	-5	30.8	28.3	0.67	-8	37.9	35.2	0.65	-7	23.9	25.1	0.59	5	26.9	25.0	0.58	-7
$PM_{2.5}$																					
Rishiri	8331	8.6	8.7	0.54	0																
Sado	6517	11.0	13.4	0.53	21	8.1	7.4	0.78	-8	9.2	9.2	0.56	0	7.2	11.5	0.54	59	10.0	6.7	0.31	-33
Oki	8410	13.1	15.0	0.64	14	8.5	9.8	0.60	14	14.4	16.1	0.63	12	11.4	16.8	0.47	48	9.1	9.1	0.24	0
Average	23258	10.9	12.3	0.61	12	13.0	12.9	0.77	-1	17.4	18.7	0.64	8	12.1	18.3	0.55	51	10.1	10.0	0.39	-1

Table 2. Same as Table 1 but for CNEMC sites.

Sites	Samples	ANN				DJF				MAM				JJA				SON			
		Obs	Sim	R	NMB	Obs	Sim	R	NMB	Obs	Sim	R	NMB	Obs	Sim	R	NMB	Obs	Sim	R	NMB
PM$_{10}$																					
Qingdao	7622	107.0	108.6	0.61	1	131.0	124.3	0.76	-5	117.3	109.9	0.49	-6	83.6	108.4	0.64	30	97.1	101.4	0.59	4
Shanghai	7581	73.4	70.5	0.55	-4	93.9	81.1	0.72	-14	83.2	80.2	0.58	-4	59.6	64.0	0.37	7	64.8	60.6	0.43	-7
Fuzhou	7610	63.7	63.8	0.38	0	69.9	72.9	0.30	4	69.8	72.6	0.32	4	55.3	45.8	0.28	-17	60.5	64.5	0.30	7
Average	22813	81.6	80.7	0.65	-1	98.4	92.6	0.74	-6	89.9	86.7	0.58	-4	66.0	72.0	0.61	9	74.1	75.4	0.51	2
PM$_{2.5}$																					
Qingdao	7627	55.2	48.7	0.72	-12	75.1	67.8	0.83	-10	56.3	43.7	0.61	-22	40.5	42.8	0.60	6	48.2	43.9	0.74	-9
Shanghai	7724	51.9	51.8	0.62	0	68.0	59.6	0.80	-12	57.2	57.5	0.60	0	42.6	49.8	0.46	17	42.6	42.9	0.51	1
Fuzhou	7641	32.3	30.0	0.44	-7	40.3	40.2	0.25	0	35.8	36.8	0.37	3	24.0	15.8	0.38	-34	29.2	27.3	0.29	-7
Average	22992	46.6	43.4	0.70	-7	61.1	55.8	0.78	-9	49.7	45.6	0.63	-8	35.6	35.5	0.62	0	39.9	38.0	0.62	-5

Table 3. Performance statistics for BC and OC from the two research campaigns in 2014. BC and OC were measured on Dongfanghong II during the spring campaign whereas only OC were collected on KEXUE-1 during the early summer campaign. Mean observation (Obs), mean simulation (Sim), correlation coefficient (R), and normalized mean bias (NMB in %) are listed. The modeled concentrations of marine-OC (including MPOA and MSOA) and its contribution to total OC were estimated.

	Dongfanghong II			KEXUE-1	
	BC	OC	Marine-OC (% in OC)	OC	Marine-OC (% in OC)
Samples	19	19		51	
Obs (μg m^{-3})	0.49	1.2		4.3	
Sim (μg m^{-3})	0.55	1.1	0.33 (29%)	3.7	0.23 (6%)
R	0.87	0.66		0.75	
NMB (%)	13	-5		-13	

Table 4. Comparison of model simulated and observed seasonal OC concentrations (unit: μg m^{-3}) at Huaniao Island and Okinawa. The modeled concentrations of marine-OC and its contribution to total OC were estimated. ANN=annual, DJF=December-January-February, MAM=March-April-May, JJA=June-July-August, and SON=September-October-November.

		Time	ANN[c]	DJF	MAM	JJA	SON	Reference
OC								
Huaniao Island	Obs	Oct 2011~ Aug 2012	3.3	4.7	3.7	1.1	3.8	Wang F. W. et al., 2015
	Sim	2014	3.2	4.5	3.9	1.7	2.9	
	Marine-OC (% in OC)		0.6 (19%)	0.56 (12%)	0.88 (22%)	0.32 (19%)	0.65 (23%)	
Okinawa	Obs	Oct 2009~ Oct 2010	1.8	1.5	2.4	1.8	1.4	Kunwar and Kawamura, 2014
	Sim	2014	1.3	1.4	1.9	0.6	1.2	
	Marine-OC (% in OC)		0.21 (17%)	0.25 (18%)	0.32 (17%)	0.06 (10%)	0.23 (18%)	

a: The location of Huaniao Island is 30.86°N, 122.67°E.

b: The location of Okinawa Island is 26.15°N, 128.03°E.

c: The annual means are averages of the four seasonal means.

Table 5. Comparison of model simulated and observed monthly mean OC concentrations (unit: μg m⁻³) at Chichijima Island. Marine-OC concentration and its contribution to total OC were estimated.

Month	Jan	Feb	Mar	Apr	May	Jun	Jul	Aug	Sep	Oct	Nov	Dec	Annual
Obs[a]	0.80	0.95	1.1	0.77	0.80	0.74	0.58	0.63	0.60	0.62	0.75	0.73	0.76
Sim[b]	0.95	1.0	1.0	1.4	1.2	0.64	0.34	0.44	0.84	0.37	0.50	0.71	0.78
Marine-OC	0.17	0.11	0.15	0.22	0.19	0.06	0.04	0.04	0.07	0.12	0.14	0.19	0.13
(% in OC)	(18%)	(11%)	(15%)	(16%)	(16%)	(9%)	(11%)	(9%)	(8%)	(33%)	(28%)	(27%)	(16%)

a: Observations at Chichijima Island (27.07°N, 142.22°E) were obtained from Boreddy et al. (2018) and are 12-yr averages (2001-2012).

b: Simulations are for the year 2014.

Table 6. Performance statistics for hourly AOD (unitless) at AERONET sites for the year 2014. Mean observation (Obs), mean simulation (Sim), correlation coefficient (R), and normalized mean bias (NMB in %) are listed. IDs are marked in Figure 1.

ID	Site	Obs	Sim	R	NMB	Samples
1	Ussuriysk	0.22	0.21	0.41	-6	945
2	Yonsei_University	0.48	0.37	0.67	-23	1629
3	Gwangju_GIST	0.33	0.36	0.53	7	900
4	EPA-NCU	0.38	0.39	0.43	4	685
5	Chen-Kung_Univ	0.49	0.37	0.60	-25	657
6	Fukuoka	0.28	0.34	0.50	18	1144
7	Shirahama	0.26	0.31	0.40	19	752
	Average	0.36	0.34	0.54	-6	6712

Table 7. Modeled domain and annual/seasonal mean MPOA emission rates, surface sea water chlorophyll-a (Chl-a) concentrations, and sea salt emission fluxes over the western Pacific of East Asia (Mean), the region including the East China Sea, the Yellow Sea, and the Bohai Sea (EYB) and the region including northern parts of western Pacific to the northeast of Japan (NWP).

	MPOA emission ($\times 10^{-2}$ µg m^{-2} s^{-1})				Chl-a concentration (mg m^{-3})			Sea salt emission flux (µg m^{-2} s^{-1})		
	Mean[a]	Max[b]	EYB[c]	NWP[d]	Mean[a]	EYB[c]	NWP[d]	Mean[a]	EYB[c]	NWP[d]
ANN	0.16	1.8	0.65	0.40	1.2	3.5	0.96	0.36	0.18	0.59
DJF	0.18	3.6	1.2	0.33	0.67	3.2	0.37	0.63	0.35	1.1
MAM	0.17	2.5	0.41	0.43	0.97	4.0	1.1	0.30	0.11	0.61
JJA	0.08	1.9	0.12	0.29	1.1	3.1	0.90	0.14	0.04	0.15
SON	0.20	3.5	0.88	0.54	1.1	2.9	0.90	0.38	0.24	0.53

a: Mean over oceanic areas.

b: Maximums over oceanic areas.

c: Ocean areas within 27~40°N, 115~123°E.

d: Ocean areas within 35~55°N, 140~160°E.

Table 8. Modeled domain and annual/seasonal mean near surface MOA concentrations, MSOA concentrations, and MOA to total OA ratios over the western Pacific of East Asia (Mean), the EYB region, and the NWP region.

	MOA concentration ($\mu g\ m^{-3}$)				MSOA concentration ($\times 10^{-3}\ \mu g\ m^{-3}$)				MOA/OA (%)			
	Mean[a]	Max[b]	EYB[c]	NWP[d]	Mean[a]	Max[b]	EYB[c]	NWP[d]	Mean[a]	Max[b]	EYB[c]	NWP[d]
ANN	0.27	1.2	0.48	0.59	2.2	6.9	4.1	3.8	26%	62%	13%	42%
DJF	0.21	0.8	0.54	0.23	0.7	3.2	1.0	0.4	24%	57%	11%	36%
MAM	0.37	1.9	0.62	0.81	2.7	10.5	5.3	4.1	26%	69%	15%	52%
JJA	0.23	2.3	0.22	0.8	3.9	13.6	7.5	8.3	23%	69%	6%	32%
SON	0.26	1.3	0.52	0.52	1.5	4.2	2.6	2.2	32%	73%	18%	48%

a: Mean over oceanic areas.

b: Maximums over oceanic areas.

c: Ocean areas within 27~40°N, 115~123°E.

d: Ocean areas within 35~55°N, 140~160°E.

Table 9. Modeled domain and annual/seasonal mean near surface wind speed, temperature, precipitation, and relative humidity (RH) over the western Pacific of East Asia (Mean), the EYB region, and the NWP region.

	Wind speed ($m\ s^{-1}$)			Temperature (°C)			Precipitation (cm month^{-1})			RH (%)		
	Mean[a]	EYB[b]	NWP[c]	Mean[a]	EYB[b]	NWP[c]	Mean[a]	EYB[b]	NWP[c]	Mean[a]	EYB[b]	NWP[c]
ANN	4.3	2.9	4.0	19.2	15.1	8.5	6.1	2.7	8.0	78	73	83
DJF	6.4	4.5	6.9	14.0	4.5	1.0	7.0	1.8	12.4	75	67	77
MAM	3.8	2.0	3.7	16.9	13.4	5.1	4.3	2.1	7.0	79	75	84
JJA	3.0	1.9	2.5	24.0	23.2	15.8	5.1	3.5	3.7	83	80	94
SON	4.1	3.1	3.1	21.7	17.9	12.0	7.9	3.2	9.0	76	71	77

a: Mean over oceanic areas.

b: Ocean areas within 27~40°N, 115~123°E.

c: Ocean areas within 35~55°N, 140~160°E.

Table 10. Modeled regional and annual/seasonal mean all-sky TOA direct radiative effect (DRE) and indirect radiative effects (IRE) due to MOA, anthropogenic aerosols, and sea salt over oceanic areas of the western Pacific (WP), the EYB region, and the NWP region. The units are W m^{-2}.

	MOA			Anthropogenic			Sea salt		
	WP[a]	EYB[b]	NWP[c]	WP[a]	EYB[b]	NWP[c]	WP[a]	EYB[b]	NWP[c]
DRE									
ANN	-0.27	-0.33	-0.50	-2.8	-6.6	-2.7	-0.86	-0.56	-0.89
DJF	-0.18	-0.32	-0.21	-1.2	-3.5	-1.2	-0.93	-0.48	-0.95
MAM	-0.38	-0.34	-0.76	-2.8	-6.2	-3.0	-0.79	-0.36	-1.1
JJA	-0.28	-0.26	-0.72	-4.9	-11.0	-5.0	-0.77	-0.85	-0.79
SON	-0.26	-0.38	-0.32	-2.2	-5.5	-1.4	-0.94	-0.55	-0.73
IRE									
ANN	-0.66	-0.23	-1.0	-7.7	-4.6	-8.7	-0.41	-0.08	-0.43
DJF	-0.64	-0.28	-0.57	-10.8	-4.8	-9.2	-0.43	-0.06	-0.31
MAM	-0.94	-0.21	-1.4	-9.9	-4.9	-10.7	-0.47	-0.07	-0.58
JJA	-0.36	-0.07	-0.78	-4.5	-3.7	-7.3	-0.30	-0.07	-0.46
SON	-0.70	-0.38	-1.4	-5.7	-5.1	-7.5	-0.45	-0.13	-0.37

a: Mean over oceanic areas.

b: 27~40°N, 115~123°E.

c: 35~55°N, 140~160°E.